Additive Manufacturing 55 (2022) 102822

Contents lists available at ScienceDirect

Additive Manufacturing

journal homepage: www.elsevier.com/locate/addma

Research paper

Continuous contour-zigzag hybrid toolpath for large format additive manufacturing

Minghao Bi [a], Lingwei Xia [b], Phuong Tran [a], Zhi Li [a], Qian Wan [b], Li Wang [b], Wei Shen [c], Guowei Ma [b], Yi Min Xie [a,*]

[a] Centre for Innovative Structures and Materials, School of Engineering, RMIT University, Melbourne, Victoria 3001, Australia
[b] Tianjin Key Laboratory of Prefabricated Building and Intelligent Construction, School of Civil and Transportation Engineering, Hebei University of Technology, Tianjin 300401, China
[c] Ameba Engineering Structure Optimization Research Institute, Nanjing 211800, China

ARTICLE INFO

Keywords:
Large format additive manufacturing
Continuous toolpath
Path planning
Topology optimization
3D concrete printing

ABSTRACT

Large format additive manufacturing (LFAM) has witnessed rapid development in recent years and facilitated digital fabrications of geometrically intricate structures. However, there has been limited research on toolpath optimization tailored for LFAM. This paper presents a novel framework to generate a globally continuous toolpath for both solid and partial infill designs in LFAM. For solid infill, outward contour and double offset schemes are used to generate smooth curves as the primary volume-filling paths; the remaining unfilled areas are covered by extending zigzag lines from the closest contours. Subsequently, a contour layer-wise connection is carried out based on the depth-first-search algorithm to formulate a globally continuous path. A post-processing step is also presented to optimize the coverage and curvature of the toolpath design. The concept is extended for partial infill settings by trimming and joining rectangular grid lines. Compared with other state-of-the-art methods in the literature, the proposed algorithm is superior in delivering better print quality, fewer sharp turns, and enhanced fabrication efficiency. Finally, two interesting experiments demonstrate how LFAM of topology optimized structures can benefit from the proposed continuous toolpath: topology optimized table printed from thermoplastic polyurethane (TPU) and topology optimized chair printed from 3D concrete printing (3DCP).

1. Introduction

Additive manufacturing (AM), also commonly known as 3D printing, enables the fabrication of spatially complex structures in a layer-by-layer fashion [1]. Compared with traditional manufacturing technologies, AM's characteristics of layer-wise fabrication allow greater design freedom in geometry and better product quality [1]. With ongoing development and burgeoning interests, AM has demonstrated unique potential in various industries, such as architecture [2], automotive [3], biomedicine [4], and aerospace [5]. Research has recently been drawn to the development of large format additive manufacturing (LFAM), termed for printing processes with printheads mounted onto a sizeable robotic system. In contrast to conventional AM using desktop printers, LFAM relies on robotic systems to fabricate 3D structures on an industrial scale [6]. Metal [7], thermoplastic material [8], earth material [9], and other composites [10] are commonly found in LFAM applications. Recent examples of LFAM include a wind turbine blade printed with bio-material [11], a metal 3D-printed bridge [12], and truss-shaped pillars from 3D concrete printing (3DCP) [13]. In this context, LFAM has opened opportunities for bringing automation, better precision, design customization and optimization to the aerospace and construction fields.

Despite having excellent prospects, AM still has specific design considerations to be addressed in the process planning phase to achieve the desired product quality. Examples of such considerations include part orientation, slicing strategy, overhang angle, support generation, and toolpath planning [14]. Poor consideration of these parameters may lead to surface defects, excessive printing time, waste of material, or in the worst scenario, failure of the fabrication process. Research has been undertaken from various perspectives to optimize the fabrication efficiency and quality, including adaptive and non-planar slicing [15,16], adaptive nozzle speed [17], support optimization [18,19], printers with increased degrees of freedom [20], mechanical improvement [21,22], and orientation optimization [23]. This work targets toolpath

---

* Corresponding author.
E-mail address: mike.xie@rmit.edu.au (Y.M. Xie).

https://doi.org/10.1016/j.addma.2022.102822
Received 13 February 2022; Received in revised form 29 March 2022; Accepted 8 April 2022

optimization for improved fabrication efficiency and enhanced quality in LFAM.

Analogous to a maze problem, the principle of toolpath generation is to fill a closed 2D region obtained from slicing using the shortest possible route. The performance of the constructed toolpath can be assessed from four aspects: underfilling, overfilling, number of sharp corners, and total path length. Fig. 1 illustrates typical underfilling (light green) and overfilling (yellow) areas near a sharp corner. Underfilling areas mark regions where the printed material cannot reach, resulting in porous surfaces and, correspondingly, the loss of stiffness. On the other hand, overfilling areas indicate zones where the material is printed twice, causing the build-up of pressure in the nozzle system and bulges on the surface. However, it should be noted that a small amount of overfilling might strengthen the bonding between filaments; it may also reduce the size of nearby underfilling thanks to the flowability of viscous material. The mechanism of robotic movement systems necessitates the deceleration of the printhead near sharp corners. Consequently, sharp turns signify a prolonged printing time and inconsistent printing widths, which should be avoided. For robotic arm setups used in LFAM, sharp turns are generally treated as rounded paths (blue dotted lines in Fig. 1) by the robotic operating system to ensure a more consistent movement pattern. The total path length represents the sum of movement distance when printing (toolpath length) and not printing (travel length). Proportional to the printing time, a minimized total path length is highly desirable for better fabrication efficiency. On this basis, an optimal toolpath seeks maximal coverage of the region using the shortest route while minimizing the presence of sharp corners and overfilling areas.

Commonly used filling strategies can be classified into three categories: direction-parallel paths, contour-parallel paths, and space-filling curves. Line path and zigzag path (Fig. 2a and Fig. 2b) belong to the direction-parallel group. Due to their simplicity and the seamless alignment of straight lines, direction-parallel paths are widely adopted in applications with a more regular profile. The line path approach suffers from frequent start-and-stops, which add extra printing time and create possible defects near the ends of lines. As an improved variation, zigzag path achieves better continuity by connecting consecutive lines. However, the formed sharp corners create serrated edges, resulting in inconsistent nozzle movement speed and staircase effect near boundaries. Formed by offsets at a constant Euclidean distance, the contour-parallel path (Fig. 2c) is another scheme widely adopted in commercial path planning packages. By offsetting iteratively from boundaries, the contour-parallel path generates smooth curves with great alignment to the border profile. However, underfilling or overfilling areas are created in the interior space when the member size is not multiple of the nozzle diameter. The disconnection between contours means extra travel time and lowered fabrication efficiency. The spiral path, Fermat spiral path, and Hilbert path (Fig. 2d, Fig. 2e, and Fig. 2f) are in the group of space-filling curves. The spiral path and Fermat spiral path essentially join contours into a locally continuous path, while the Hilbert path fills a region with a repeatable rectangular pattern. However, both the spiral path and Fermat spiral path still fall victim to contour-parallel path's problem — potential underfilling and overfilling of skeletal regions. Similar to zigzag path, the frequent presence of sharp corners degrades the print quality of Hilbert path. In this setting, a globally continuous path with a smooth trajectory and optimal coverage is preferred for maximizing print quality and efficiency.

This paper proposes a novel toolpath development framework to construct a globally continuous toolpath for LFAM. As shown in Fig. 3, the algorithm takes a hybrid approach by exploiting the concepts of both contour-parallel and zigzag toolpaths. Outward contours and double offset are used to generate smooth curves as the primary volume-filling paths; this fundamentally leverages the contour-parallel path's benefits in creating smooth paths while circumventing its drawback in forming sharp corners, underfilling and overfilling areas near the centrelines. The remaining unfilled areas are covered by extending zigzag lines locally from the closest contours. Subsequently, a layer-wise connection will be carried out based on the depth-first-search (DFS) algorithm to formulate a globally continuous path. A post-processing step is also presented to optimize the coverage and curvature of the toolpath design. As a supplement to paths for solid infill, a globally continuous toolpath method for partial infill is developed to reduce structural weight without sacrificing continuity (Fig. 4).

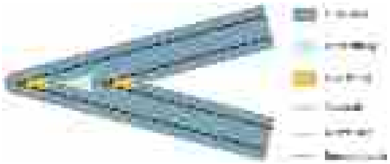

Fig. 1. Underfilling and overfilling areas near a sharp corner.

The main contributions of this paper are summarised as follows:

- An algorithm to generate a globally continuous toolpath to improve print quality and save printing time and material.
- The proposed hybrid method exploits the advantages of both contour-parallel path and zigzag path while minimizing their disadvantages.
- Methods from the literature focus on small-scale AM, such as fused deposition modeling (FDM), which generally requires a small nozzle size to achieve good print quality. When applied to LFAM, the proposed method has shown better performance in print quality.
- Apart from solid infill, a globally continuous toolpath for partial infill is also presented and tested from experiments.
- Two interesting experiments demonstrate how LFAM of spatially complex structures can benefit from a globally continuous toolpath: topology optimized table printed from thermoplastic polyurethane (TPU) and topology optimized chair printed from 3DCP.

The remainder of the paper is organized as follows: Section 2 reviews some related work in the literature about LFAM and path planning strategies. Section 3 describes the proposed method for generating a globally continuous toolpath for solid and partial infill. Digital results and comparison to state-of-the-art methods are presented in Section 4, followed by experimental validation and concluding remarks in Sections 5 and 6.

2. Related work

This section reviews the related work in LFAM and different toolpath strategies in the literature. The compatibility between LFAM and continuous toolpath and the limitations of the existing algorithms are summarized. For more details on recent developments in path planning strategies, interested readers are referred to the following review [28].

2.1. Recent developments in LFAM

In line with the concept of digital fabrication, LFAM has been extensively studied and implemented in industrial practices. Some recent applications of LFAM in the construction field include 3D-printed bending-active formwork using plastic ABS [29], metal 3D-printed footbridge using stainless steel [12], and 3D printed concrete green wall [30].

Compared with AM using desktop printers, LFAM typically employs large-scale robotic systems to control printhead movement. Multi-axis robotic arms [31,32] are effectively used to position the printhead installed at the forepart of the robotic arm. Multiple robotic arms can work collaboratively to expedite the printing process [31]. By mounting the robotic arm onto a mobile platform, a mobile printing system [33] significantly improves mobility and can operate in situ. Gantry [34] and cable-suspended systems [35] rely on an external frame to control the movement of the printhead. Compared with robotic arm systems, gantry

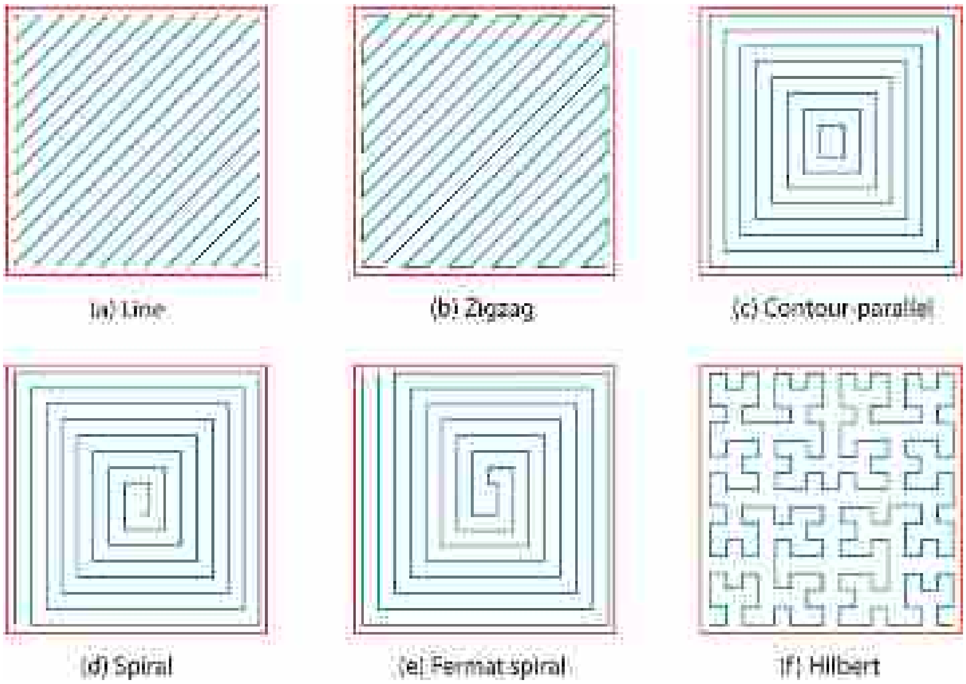

Fig. 2. Six filling patterns: (a) line; (b) zigzag; (c) contour-parallel; (d) spiral [24,25]; (e) Fermat spiral [26]; (f) Hilbert [27]. The red line represents the boundary of the region to be filled.

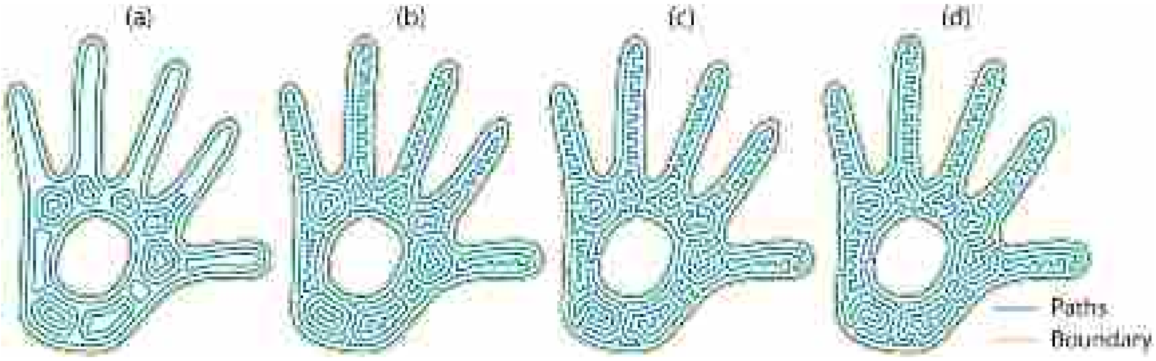

Fig. 3. An overview of the proposed method for generating a continuous toolpath for solid infill: (a) smooth contours are generated based on the outward contour and double offset schemes; (b) zigzag lines are formed to fill local underfilling areas; (c) global continuity is achieved by connecting toolpaths based on the DFS algorithm; (d) the toolpath is post-processed to optimize its curvature.

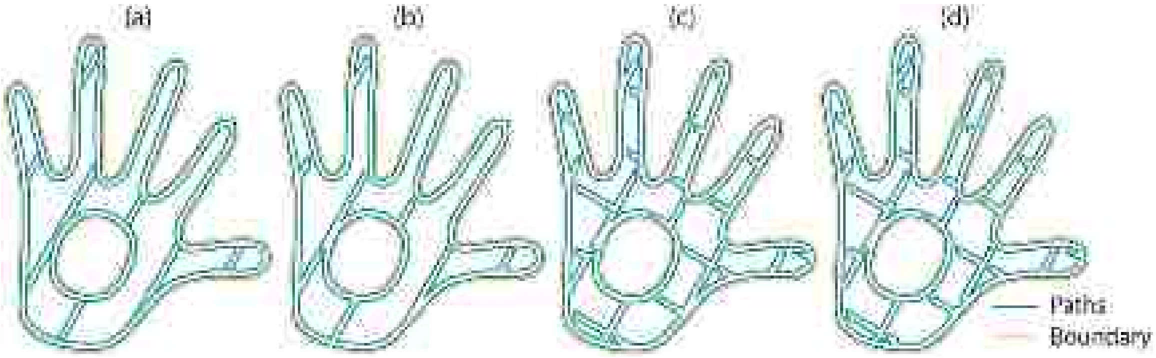

Fig. 4. An overview of the proposed method for generating a continuous toolpath for partial infill: (a) gridlines are generated within the boundary offsets; (b) gridlines are trimmed and connected to the boundary offsets; (c) repeat in the orthogonal direction; (d) zigzag operation is performed to cover small gaps.

and cable suspended systems are relatively inexpensive and have better precision but are restricted in scale and mobility. For more details on printing systems in LFAM, interested readers are referred to a review [36].

Depending on the material and application, the nozzle size for LFAM generally ranges from 1 mm (for TPU and ABS materials) to more than 30 mm (for concrete and earth materials). The numerical control unit of robotic systems typically approximates curves as a collection of points, the toolpath for 3D printing is interpreted as sets of linear segments. On this basis, if the printing is kept at a constant feed rate, severe discontinuities in velocity and acceleration occur near junction points. In an attempt to achieve smooth and consistent motion, modern control units often have an in-built interpolation scheme to smooth sharp corners [37]. For LFAM, the material feeding system is generally separated from the robotic control system; simultaneous start-and-stop action of both systems can be challenging. In this scenario, the process planning for LFAM calls for a continuous toolpath to maximize print quality and efficiency.

In recent years, 3DCP has been one of the most popular LFAM technologies and has demonstrated promising potential in large-scale digital construction [38]. Research on 3DCP has been extensively conducted in terms of material [39,40] and applications [41,42]. Studies have shown that the printability of 3DCP is interrelated with the rheological properties of fresh concrete paste [40,43] and the mechanical properties of 3DCP are interrelated with toolpath patterns [44]. An optimal setting time is crucial to maximizing layer-to-layer bonding without blockage of the nozzle due to concrete paste's solidification. In this regard, having a continuous toolpath can improve the printability of 3DCP and reduce the risk of blockage. For more details on 3DCP, interested readers should refer to a recent review [43].

2.2. Direction-parallel paths

Thanks to the simplicity and excellent computational efficiency, direction-parallel paths (line and zigzag paths) are commonly used in AM applications. Research on direction-parallel paths focuses on optimizing path orientation, width, and continuity. To alleviate the problem of the staircase effect near boundaries, direction-parallel paths in the literature generally arrange layers of contours near borders and place zigzag within the contours [17,45–48]. Jin et al. [17] developed a zigzag toolpath algorithm with adaptive printing speed to reduce build time and improve geometrical accuracy. Jin et al. [47] proposed a zigzag generation algorithm with an optimal inclination angle and minimal sub-paths.

Recent studies attempted to obtain a globally continuous toolpath based on direction-parallel paths. Dwivedi and Kovacevic [49] presented an automated torch path planning approach; a continuous toolpath is obtained by connecting individual zigzag paths filled in each decomposed sub-region. Ding et al. [45] improved the methodology by identifying an optimal scan direction in each decomposed polygon. A similar approach was presented by Jin et al. [46], with two outer contours for better alignment to the boundaries. Decomposition in previous work requires boundaries with simple geometry; Xia et al. [48] developed an algorithm to produce a globally continuous path for arbitrary boundary shapes using the double zigzag path. Overall, direction-parallel based algorithms are favorable for their simplicity, computational efficiency, and alignment of straight lines but fall victim to sharp corners and staircase effect near transition zones.

2.3. Contour-parallel paths

Compared with direction-parallel paths, contour-parallel paths feature the generation of smooth curves with a great match to the boundary profile. The foundation for creating contour-parallel paths is the offset operation of the boundaries. Different methods have been proposed in the literature and can be generally classified into four categories: Voronoi diagram [50–52], level-set method [53], edge offset [54–56], and vertex offset [57,58]. Developed based on published work [59,60], the Clipper library [61] is an online open-source package for planar curve offset and can be used for the efficient generation of contours.

The main shortcoming of contour-parallel paths is the presence of underfilling and overfilling areas in the interior space in two scenarios. Firstly, when the dimension of the 2D region is not a multiple of the nozzle size, the innermost contours may be too close or apart from each other. Secondly, sharp boundaries are inherited during the offset operation, accumulating into underfilling and overfilling areas due to the bottleneck effect. To alleviate the problems from sharp corners, Lin et al. [62] introduced dual offset and clear-up toolpath procedures to alter the path; the resulted path exhibited a noticeable decrease in the level of sharpness. To achieve a better coverage rate, Xu et al. [63] developed an image-processing-based technique to generate contours using the shortest Euclidean distance (SED) image with a Gaussian filter.

In pursuit of a globally continuous path from the contour methodology, Zhao et al. [26] suggested using connected Fermat spirals (CFS) for layered fabrication. This method decomposed contours into sub-regions and created a locally continuous Fermat spiral in each sub-region; continuity was later achieved by rerouting and connecting the Fermat spirals. Zhai and Chen [64] further extended this method to generate paths for porous structures; a closed 2D region was segmented using the Voronoi diagram, followed by the generation of Fermat spiral paths in subdomains and their sequential connection. Inside a complex 2D geometry, contour-parallel paths are better for volume-filling than direction-parallel paths thanks to their smoothness and match with intricate boundary shapes. However, continuous path algorithms in the literature still have sharp corners and underfilling areas that need to be improved.

2.4. Space-filling curves

Different types of space-filling curves have been proposed in the past. Spiral paths [24,25] were commonly applied in numerically controlled machining thanks to their smoothness. Griffiths [27] proposed a toolpath strategy based on Hilbert's curve for machining curved surfaces. A more recent study based on Hilbert's curve was presented by Shaikh et al. [65] for FDM processes. Kuipers et al. [66] developed a framework called CrossFill to generate a self-supporting foam structure based on space-filling curves. A maze-like path generation scheme was introduced by Lin et al. [67] to enhance the mechanical properties of FDM printing. Space-filling curves can improve print quality and efficiency in various ways, but their complexity in shape may limit their computational efficiency and range of applications.

2.5. Adaptive paths

Toolpath methods introduced in the previous subsections are based on uniform filament width and layer height. Another strategy is the adaptive toolpath, where feed rate control and non-uniform layer height are used to optimize the toolpath design. Ding et al. [68] proposed an adaptive width control scheme for wire-feed AM using medial axis transformation; the toolpath with adaptive width was sampled between the medial axis and the boundaries. An alternative method was presented by Jin et al. [69] to average the spacing between paths near the medial axis. A more sophisticated strategy for adaptive width control was developed by Kuipers et al. [70], which reduced the bead width range using various beading schemes. Etienne et al. [71] used curved slicing to generate a toolpath with variable layer height to better align the object surface. Zhang et al. [72] developed a framework to deliver singularity-aware and collision-free adaptive motion control, improving the surface quality of the printed results. Overall, adaptive paths can effectively reduce underfilling and overfilling by adjusting the extrusion rate near problematic regions. However, adaptive paths add extra complexity to the toolpath design and may not be compatible with some printer systems. The nozzle movement speed limits the range of motion control, as the printer may become unstable after exceeding the maximum allowable printing speed. Optimizing toolpath geometry becomes more important for underfilling and overfilling unable to be resolved by adaptive paths.

3. Methodology

This section systematically explains the steps of the proposed hybrid method. Programming and computation are carried out on the Rhino and Grasshopper platforms. Contour lines are generated using the Clipper Library [61]; the default gap-filling type of square is chosen to allow easy identification of offsets' transition points. With a focus on LFAM, a comparatively large nozzle diameter is used for examples in this paper to test the robustness.

3.1. Volume-filling using contour paths

The first step of the hybrid method is to generate contours as the primary volume-filling paths. In Section 2, the limitations of the contour-based algorithms are identified as the presence of sharp corners due to the bottleneck effect, underfilling, and overfilling areas near the medial axis (Fig. 5a). The proposed method uses double offset and outward contour schemes to generate contours with proper alignment, thus eliminating the concerned problems.

3.1.1. Double offset

With the nozzle diameter denoted as d, the conventional contour algorithm offsets iteratively from the boundary at a Euclidean distance of $a * d$, where a represents the layer number of contours. Fig. 5a illustrates three typical problems for the conventional contour algorithm. When the dimension of an area is not multiple of the nozzle diameter d, the innermost contours can be too close (overfilling) or apart (underfilling). In transition contour layers, sharp corners tend to be formed because of the bottleneck effect.

A 2-step double offset scheme is introduced to prevent narrow paths and sharp corners. A contour is generated by offsetting inwards at a distance of 1.5d and then outwards at a distance of 0.5d. The extra distance of 0.5d avoids overlap of the printed material and the formation of small features. Fig. 6 compares the concepts from the conventional offset and double offset method; the removal of sharp corners and the bottleneck effect are noticeable.

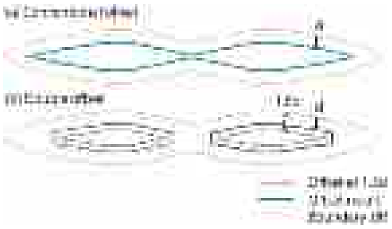

Fig. 6. Comparison between conventional offset and double offset schemes.

Given the prescribed 2D closed region R, the contour lines generated by offset are denoted as $c_{i,j}$ from the boundary ∂R, where i indicates the contour layer number and j signifies the contour index in this contour layer. Note that the contour layer number marks the offset sequence for generating contours in 2D and should not be confused with the printing layer number for slicing in 3D. For example, if two contours are obtained by offsetting the boundary, they are denoted as $c_{0,0}$ and $c_{0,1}$. Offsets on the next layer are labeled as $c_{1,0},\ c_{1,1},\ c_{1,2}\ \cdots$. The total number of contours in a contour layer is denoted as n_i. After offsetting inwards iteratively using the double offset rule, two sets of curves are determined: boundary curve set $\{S_b\}$ and center curve set $\{S_c\}$. The boundary curve set $\{S_b\}$ is determined as the outermost contour lines with geometrical similarities:

$$S_b = \left\{ c_{i,j} \mid (1-\alpha)\langle \frac{l(c_{i+1,\,j})}{l(c_{i,\,j})} < (1+\alpha) \text{ and } n_i = n_{i+1} \right\} \tag{1}$$

where $l(c_{i,j})$ denotes the length of the contour $c_{i,j}$ and α is a user-defined threshold to measure the similarity between contours in successive layers. The value of α should be kept below 0.2 to ensure resemblance between contours and avoid underfilling; in this paper, α is chosen as 0.15. The number of contour layers in $\{S_b\}$ is recorded as $i_{b,max}$. Centre curve set $\{S_c\}$ identifies the innermost contours where no further offset with a distance of 1.5d can be carried out. The contour layer number i of each center curve is recorded to be used in the next step. Fig. 5b presents the result produced by the double offset strategy, with $\{S_b\}$ and $\{S_c\}$ highlighted in blue and pink, respectively. For four contours in $\{S_c\}$, A, B, and C are on contour layer four and D is on contour layer three. With

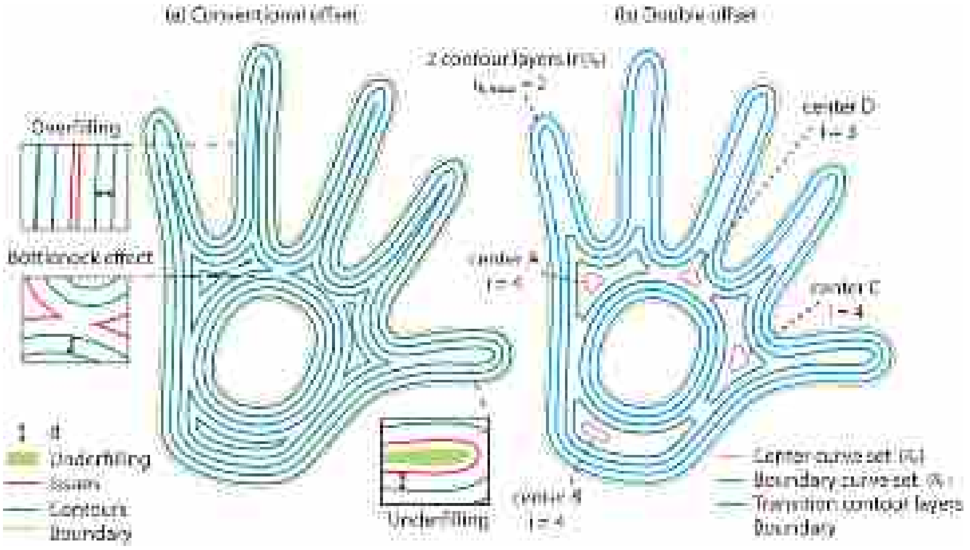

Fig. 5. Comparing results generated using conventional offset and double offset schemes: (a) conventional offset algorithm leads to three problems: overfilling, underfilling and sharp corners due to the bottleneck effect; (b) result from double offset prevents overfilling and sharp corners but generates underfilling areas. Blue and pink curves highlight the boundary curve set $\{S_b\}$ and the centre curve set $\{S_c\}$, respectively.

two contour layers in $\{S_b\}$, the value of $i_{b,max}$ equals two. Results obtained using the double offset method replace sharp corners and narrow regions with gaps. In transition contour layers (contour layers two and three in Fig. 5b), the generated contours lose the desired characteristics of being aligned and parallel. In this context, an outward contour scheme is introduced to restore parallelism between offsets.

3.1.2. Outward contour

With the innermost contours identified in $\{S_c\}$ as input, the outward contour scheme fills the space by generating offsets towards the boundary. Again, this strategy prevents sharp corners and ensures that each contour can be tightly spaced to the contour on the previous layer. To generate contours outwards, all intermediate curves except $\{S_b\}$ and $\{S_c\}$ are removed. To cover the space between $\{S_b\}$ and $\{S_c\}$, each center curve is offset by $(i - i_{b,max})$ times at a distance of d to form tightly spaced contours. Here $i_{b,max}$ is deduced to avoid overlap between the new offsets and existing contours in $\{S_b\}$. The result is shown in Fig. 7a; By deducting $i_{b,max}$ as two, center curves on the third (D) and fourth layers (A, B, and C) are offset by one and two times, respectively.

The steps above are repeated for the remaining unfilled area until no more contours can be created. The final result is illustrated in Fig. 7b. After generating offsets in this step, the interior space is predominantly covered with equally spaced contours without overfilling areas. The remaining local underfilling areas are filled by the zigzag operation in the next step.

3.2. Fill local gaps using zigzag paths

Following the previous step, local underfilling areas are filled by zigzag paths using five steps (Fig. 8). The first step is to find potential underfilling areas by offsetting the contours at a distance of $0.5d$. With square as the fillet type, polylines created by the offset operation have clear transition points. Those points are identified for corners where the angle change is larger than 120° (illustrated as feature points in Fig. 8a). The outline of the underfilling area can then be split into segments, where each segment corresponds to a close edge suitable for zigzag connections. In Fig. 8a, the outline in the red dashed line can be split into three segments. The most extended segment is selected as the most suitable side to connect the zigzag path and removed from the outline. The rest of the outline, noted as e_r, is offset by a distance of $0.5d$ and extended to the closest boundary to form a closed region for zigzag connection. In Fig. 8b, the red dashed line is e_r after removing the longest segment. The blue area is the closed zigzag region, with A and B representing the intersection points with the closest contour. The direction of the zigzag lines, $\overrightarrow{z}$, is perpendicular to the vector betweem A and B, $\overrightarrow{AB}$. The number of zigzag lines, n_z, is the rounded value of the distance between A and B divided by the nozzle diameter d:

$$n_z = \text{round}(\frac{l_{AB}}{d}) \tag{2}$$

n_z is further reduced by one if it is an odd number. By doing so, both endpoints of the zigzag path can be placed on the closest contour. Illustrated as the purple path in Fig. 8c, the zigzag lines are spanned along the direction $\overrightarrow{AB}$ at a distance of d, and connected based on the odd-even rule. The new zigzag path is then merged with the closest contour (Fig. 8d).

The zigzag operation is an iterative process. The first zigzag operation can cover most of the underfilling regions, but there are still minor underfilling areas (red areas in Fig. 8d) because of two reasons: (1) the number of the zigzag lines may be rounded down; (2) turning points of zigzag lines create a staircase effect. In this paper, underfilling areas whose outline is shorter than $3 * d$ is considered insignificant and neglected; larger underfilling areas can be minimized by performing another zigzag operation. An underfilling area is considered to be narrow if the length of $|\overrightarrow{AB}|$ is less than d. For such locations, the boundary of the zigzag region can be directly merged to the closest contour without needing zigzag lines (modified areas in Fig. 8e). After the second zigzag operation, the remaining underfilling areas are generally negligible triangular regions (red areas in Fig. 8e) and are further reduced in the post-processing step. All results in this paper are obtained by performing two rounds of zigzag operations. The palm example after the zigzag operation is shown in Fig. 9, leading to good coverage without highly sharp corners.

3.3. Connection of layered paths

The next step is to connect the layered paths into a globally continuous path. The connection consists of three steps: contour layer-wise connection, group-wise connection, and boundary connection.

3.3.1. Contour layer-wise connection

Paths generated from the outward contour scheme are closely spaced with a clear contour layer-wise relationship. Each curve can be linked to a single parent curve in the preceding layer based on this relationship. A parent curve can be associated with multiple child curves in transition

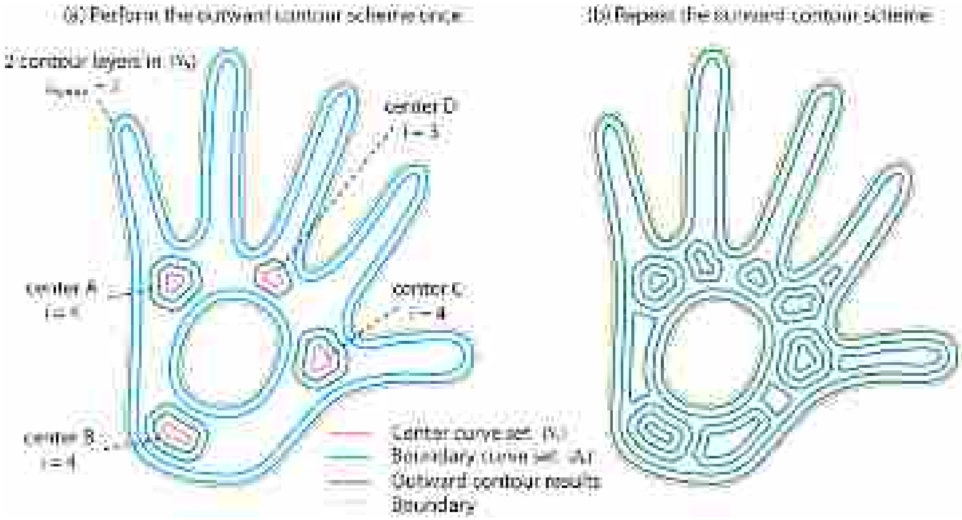

Fig. 7. The results after performing the outward contour scheme: (a) the outward contour scheme is performed for the first time, and each center curve generates tightly spaced contours outwards; (b) the result after repeating the outward contour scheme. The interior space is predominantly covered by tightly spaced contours.

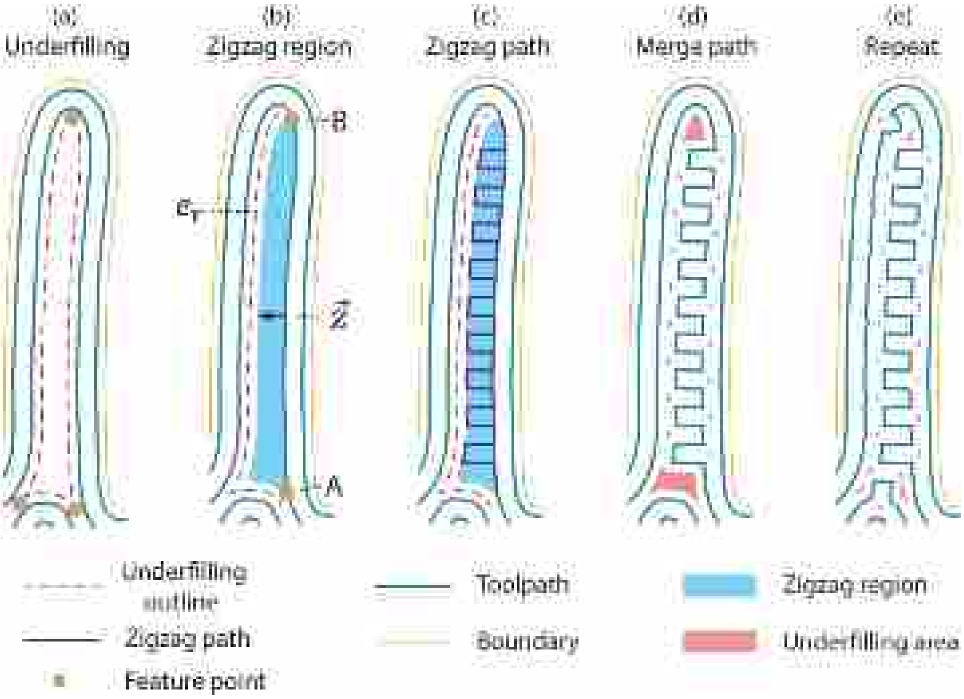

Fig. 8. Five steps for filling local underfilling areas with zigzag paths.

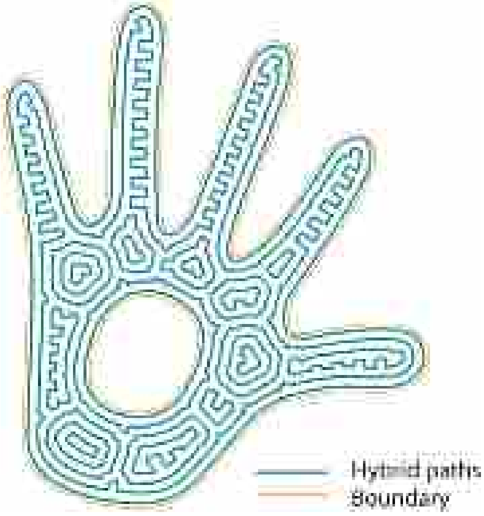

Fig. 9. Hybrid paths are obtained by combing contours with zigzag paths in this step. Zigzag paths are extended locally from the closest contours to cover underfilling areas.

contour layers. In this case, the DFS algorithm is applied to locate the most suitable parent curve in the previous contour layer. To avoid duplicate connections, examined child curve should not be visited twice.

The connection route between a parent curve $c_{i,j}$ and child curve on the next contour layer $c_{i+1,j'}$ is determined based on three preferences: 1. shortest distance between two successive contour layers; 2. the connection points are preferred on curve segments with long span and low curvature; 3. If possible, connection points are joined to existing routes to minimize new corners. The three preferences above are realized by a point-wise approach. By placing point candidates along the curve $c_{i,j}$, the distance between a point $p_{i,k}$ (i and k denotes the contour layer number and point index, respectively) and curves in the next contour layer are evaluated to locate the closest parent curve $c_{i+1,j'}$. If both $p_{i,k}$ and the projected point $p_{i+1,k}$ have low curvature, the connection line is found by linking $p_{i,k}$ and $p_{i+1,k}$. Two straight lines, parallel and $0.5d$ away from the connection line, are created as entry and exit routes. For the third preference, existing connection points are recorded in a separate list to be evaluated in priority. Fig. 10 demonstrates how the connection is made between three consecutive contour layers. Note how previous connection points are reused to minimize the number of transitions.

Fig. 10. Illustration of how connection routes are found between contour layers. The contours are generated from $\{S_c\}$ based on the outward contour scheme, the layer-wise relationship is used to identify the connection sequence.

3.3.2. Group-wise connection

After performing the contour layer-wise connection, discontinuous paths are joined into locally continuous groups, with the group number equal to the boundary number. By using a similar point-wise approach, each group is connected to the closest neighboring group on their outermost contour layer. The search is repeated until all groups within the boundary contour layer are merged into a continuous path. Note that the outermost contour layer, exemplified as two boundary contours in pink in Fig. 11a, is omitted from the search at this stage. In Fig. 11a, two colorized groups are connected via the red routes.

3.3.3. Boundary connection

The connection of the boundary is placed as the last step to avoid forming multiple corners on the boundaries. To maximize the smoothness and integrity of the boundary profile, each boundary curve is

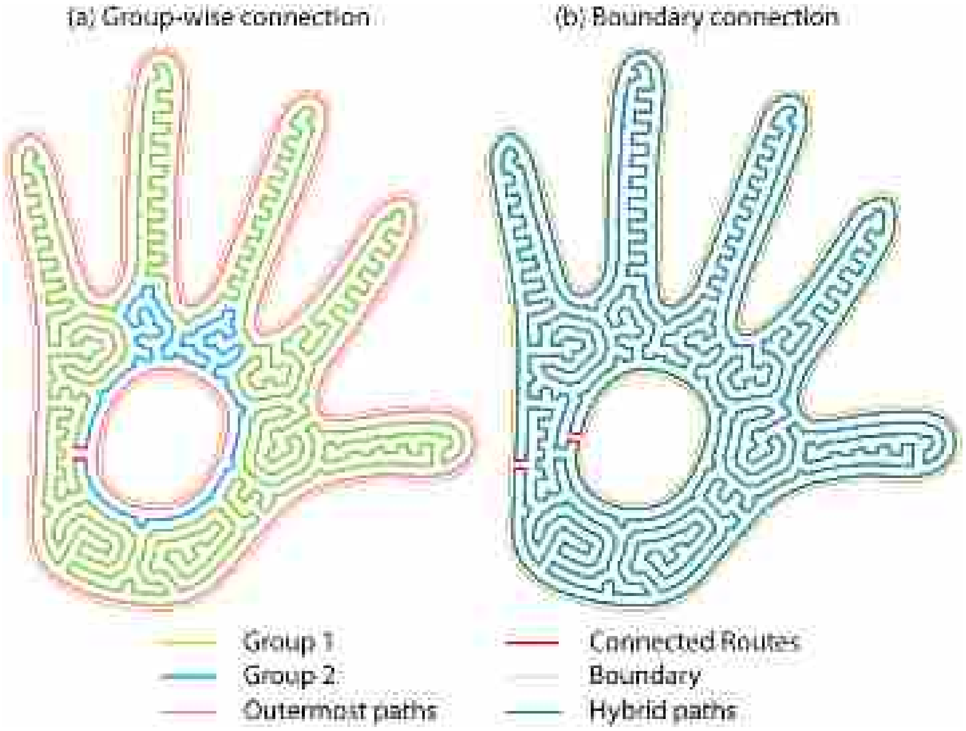

Fig. 11. (a) Locally continuous groups (green and blue) are connected based on the same principle described in previous steps. Outermost contours (pink) are omitted at this stage to avoid forming multiple corners on the boundary contour layer. (b) The last step is connecting the outermost contours to the continuous inner path. Each boundary contour is connected only once (red routes) to minimize the number of corners on the boundary profile.

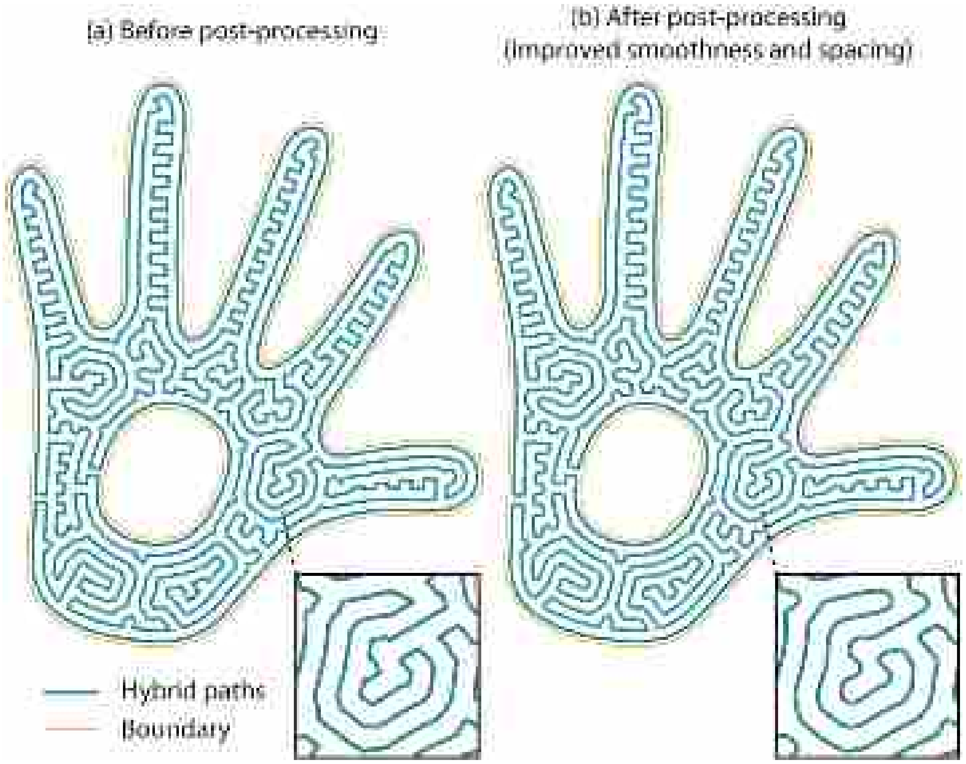

Fig. 12. Comparison of the result before and after post-processing. After post-processing, the toolpath has an improved overall smoothness and a more even spacing.

connected to the continuous inner path only once. Unlike connection routes in previous steps, the distance between the entry and exit routes for boundary connection is set as a reduced value: $\beta * d$. The value of β has a range of 0–1 and depends on the material and speed of the nozzle. The movement of the nozzle may drag the material, creating gaps on the profile and thus reducing the bonding strength. Having a reduced distance allow overlaps of the material, which increases bonding and smoothness of the boundaries. In this paper, the value of β is set as 0.7. After boundary connection, a globally continuous toolpath is constructed (Fig. 11b).

3.4. *Post-processing optimization*

A post-processing algorithm is proposed to increase the smoothness of the path and adjust its spacing in crowded areas. The path is firstly sampled at a uniform spacing, and the location of the sampled points is sequentially adjusted based on its neighboring conditions. Underfilling is reduced by moving the closest points of the path towards the centroid of nearby unfilled areas. Subsequently, a filter-based approach detects points near overfilling regions and sharp corners and adjusts their position to a more evenly distributed fashion. Implementation of the post-processing algorithm can be found in Appendix. A comparison of the results before and after post-processing can be found in Fig. 12. While the topology of the toolpath remains unchanged, the post-processing step brings a noticeable improvement in overall smoothness.

3.5. *Toolpath for partial infill*

To save material and reduce weight, many AM applications choose partial infill (non-100% coverage) rather than solid infill (100% coverage). Generally speaking, a partial infill with arrayed patterns in the interior space should be used in conjunction with a solid infill to seal the top and bottom surfaces. This subsection introduces a continuous toolpath strategy for partial infill to complement the previous algorithm.

The proposed method selects the rectangular grid as the infill pattern, whose center point is matched in each layer. With the same center point, spacing of the grid s, and nozzle diameter d, the toolpath is aligned vertically to ensure continuous self-support. Defined in Eq. (3), the infill ratio I is calculated based on the grid spacing s and nozzle diameter d. A simplified example is visualized in Fig. 13; the dashed, solid, and dotted lines are the centrelines of the grid, the toolpath, and the boundaries of the unfilled area, respectively. θ is a user-defined angle that controls the grid orientation. Note that each centreline is associated with two parallel paths as the entry and exit routes, the spacing between them is kept at a distance of d.

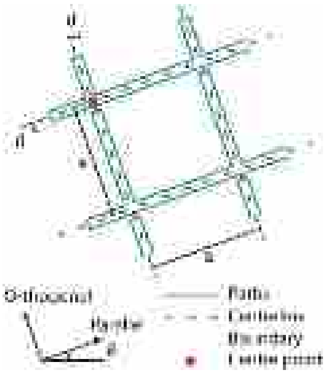

Fig. 13. An illustration of the rectangular grid used in the partial infill strategy.

$$I = \frac{s^2 - (s - 2d)^2}{s^2} \tag{3}$$

With the known value of I and d, Eq. (3) is re-arranged to calculate grid spacing value s as follow:

$$s = \frac{2d \times (1 + \sqrt{1 - I})}{I} \tag{4}$$

The first step is to offset the boundary ∂R inwards iteratively for n times, where n is a user-defined value controlling the thickness of the boundary wall. The innermost contours form a closed space to be covered by the partial infill. Grid lines in the parallel direction are first drawn and trimmed within the infill boundary. Fig. 14a shows the trimmed grid lines within two boundary offsets.

The trimmed lines are then modified on both ends to achieve continuity. The start points of the trimmed lines are joined to the infill boundary by removing the segment between them. The connections at the endpoints, denoted as A and B, are based on three different scenarios (Fig. 14b):

1. If A and B are on the same infill boundary that is connected before, and the segment length between A and B is less than $3d$, the endpoints are retreated by a distance γd. γ in this paper is set as 0.7 to allow bonding between the infill and the boundary. A straight line is added between the retreated endpoints to connect the entry and exit path.
2. If A or B is connected to an interior boundary for the first time, the interior boundary is merged with the trimmed lines.
3. If A and B are on different infill boundaries or the segment length between A and B is larger than $3d$, the endpoint of the shorter line (A) is projected onto the longer line (A′). By breaking the longer line at A′, its first-half segment is joined to the shorter line according to situation 1. The second half segment is connected to the next line of the other path.

After joining the infill paths in the parallel direction, grid lines in the orthogonal direction are trimmed and connected under the same principle (Fig. 14c). The connection between the infill and boundary offsets uses the same method as described in Section 3.3. The zigzag operation described in Section 3.2 is used to refill underfilling areas near the infill boundary (Fig. 14d).

4. Numerical studies

This section presents a variety of work cases to test the robustness of the proposed method. A comparison with algorithms in the literature is provided to show the strengths and weaknesses of our method. The algorithm is implemented on the Rhino and Grasshopper platforms on an Intel ® i7–9700 K CPU 3.60 Hz with 32 GB RAM.

4.1. *Comparison of different toolpath methods*

This subsection compares the proposed hybrid method with other toolpath strategies: the CFS method [26], the continuous zigzag method [48], conventional zigzag and contour-parallel methods. For clarity, only the results from three continuous toolpath methods are illustrated (Fig. 15); the conventional zigzag and contour-parallel methods are used to provide more statistical comparisons. The algorithm's performance is evaluated on five factors: print quality, continuity, printing time, computational time, and the number of sharp turns. Internal openings are placed inside four examples (cat, honeycomb, gear, and rabbit) to test the algorithm's robustness on complex arbitrary geometries, whereas the other two examples (letter A and M) demonstrate its application for more regular shapes. Note that some shapes have similarities with examples in previous papers [26,48,64], but the toolpaths

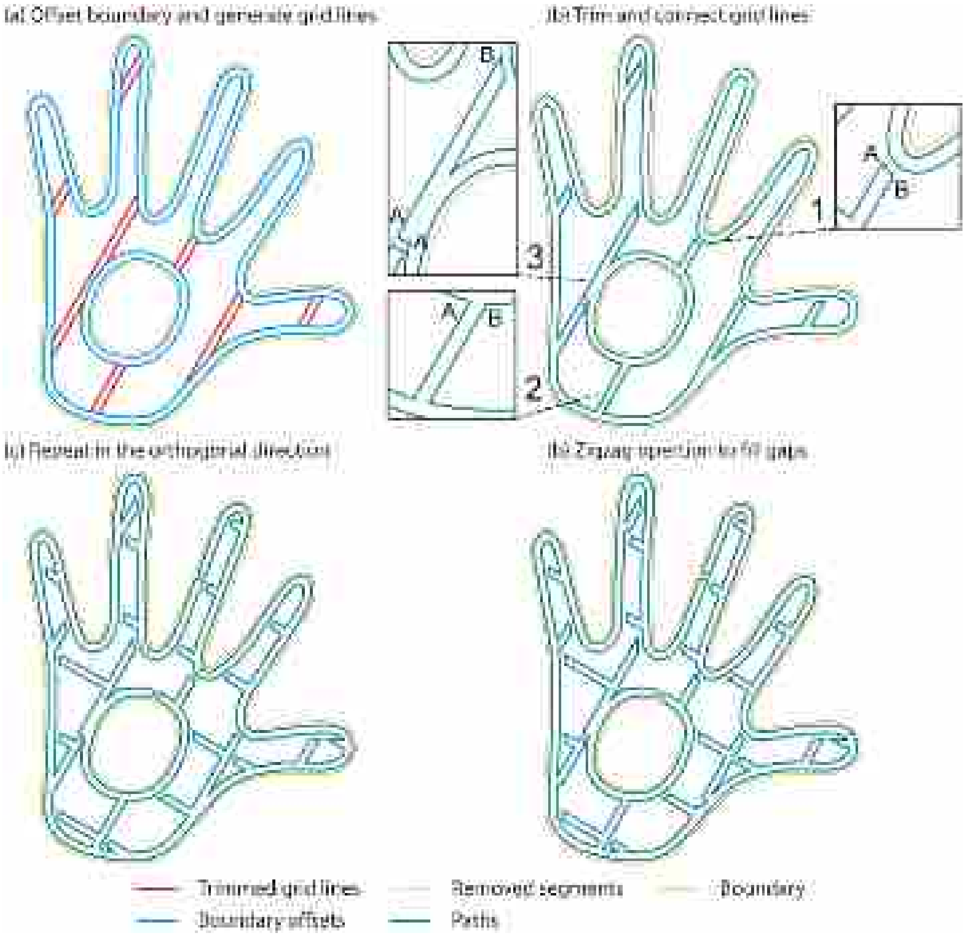

Fig. 14. Steps of the partial-infill strategy: (a) generate boundary offsets and trimmed grid lines; (b) three different situations when connecting trimmed grid lines with the infill boundary; (c) repeat the strategy in the orthogonal direction; (d) zigzag operation to fill local gaps.

are different as a larger nozzle diameter is emphasized in this paper for LFAM. For easy readability, the best result in a table is highlighted.

4.1.1. *Print quality*

As defined in Section 1, overfilling and underfilling can directly influence the print result's surface quality, material usage, and mechanical performance. Underfilling areas are obtained by offsetting the toolpath at a distance of 0.5d, while the total overfilling area is computed as:

$$l * d - A$$

where l, d and A stand for the total toolpath length, nozzle diameter, and total covered area, respectively. As shown in Table 1, the print quality is assessed based on four criteria: overfilling ratio, underfilling ratio, number of large gaps, and size of the largest gap. As suggested by the name, the overfilling and underfilling ratios represent the percentage of the overfilling and underfilling areas with regard to the total print area. Large gaps in this subsection are defined as underfilling areas whose size is greater than 0.05% of the total print area. The value of 0.05% is chosen empirically, as areas minor than this threshold are generally negligible and may be refilled by viscous material. On the contrary, larger areas are visually noticeable and susceptible to be mechanical weakness and aesthetic defects. For visualization, large gaps are colorized in red in Fig. 15.

As shown in Table 1a, the overfilling ratio of the proposed method is very comparable to the CFS method and slightly worse than the continuous zigzag method. On the other hand, the proposed method significantly reduces underfilling areas (Table 1b and c). The underfilling ratio of the proposed method is generally half of the value of other methods; the size of the largest underfilling area can be 10–20 times smaller on average (Table 1d). This improvement can be visually verified in Fig. 15 from the evenly and tightly spaced toolpaths and observed from experimental results in Section 5.

4.1.2. *Continuity*

As the main focus of this paper, the global continuity of a toolpath can reduce the printing time and improve the print quality. All three continuous toolpath algorithms manage to achieve global continuity, whereas the conventional zigzag and contour-parallel methods are overwhelmed by discontinuous path segments (Table 2a).

4.1.3. *Sharp turns*

As discussed in Section 2.1, sharp turns should generally be avoided in LFAM to bypass inconsistent movement speed and potential print defects. Previous work [58] identified a sharp turn as a point whose turning angle is less than 110°. The observation is followed in this subsection, and points are sampled on the toolpaths at an interval of $d/4$. The value of $d/4$ is chosen to prevent excessive sampled points while preserving the features and curvature of the toolpaths. The ratio between sharp corner points and total point count is calculated and reported in Table 2b. Zigzag and the continuous zigzag methods behave poorly in this criterion because of sharp turns created by the odd-even rule. Noticeable in Fig. 15, some sharp turns are created in the CFS and contour-parallel paths due to the bottleneck effect. The proposed hybrid method achieves a much better result thanks to the innovative contour schemes and the post-processing step.

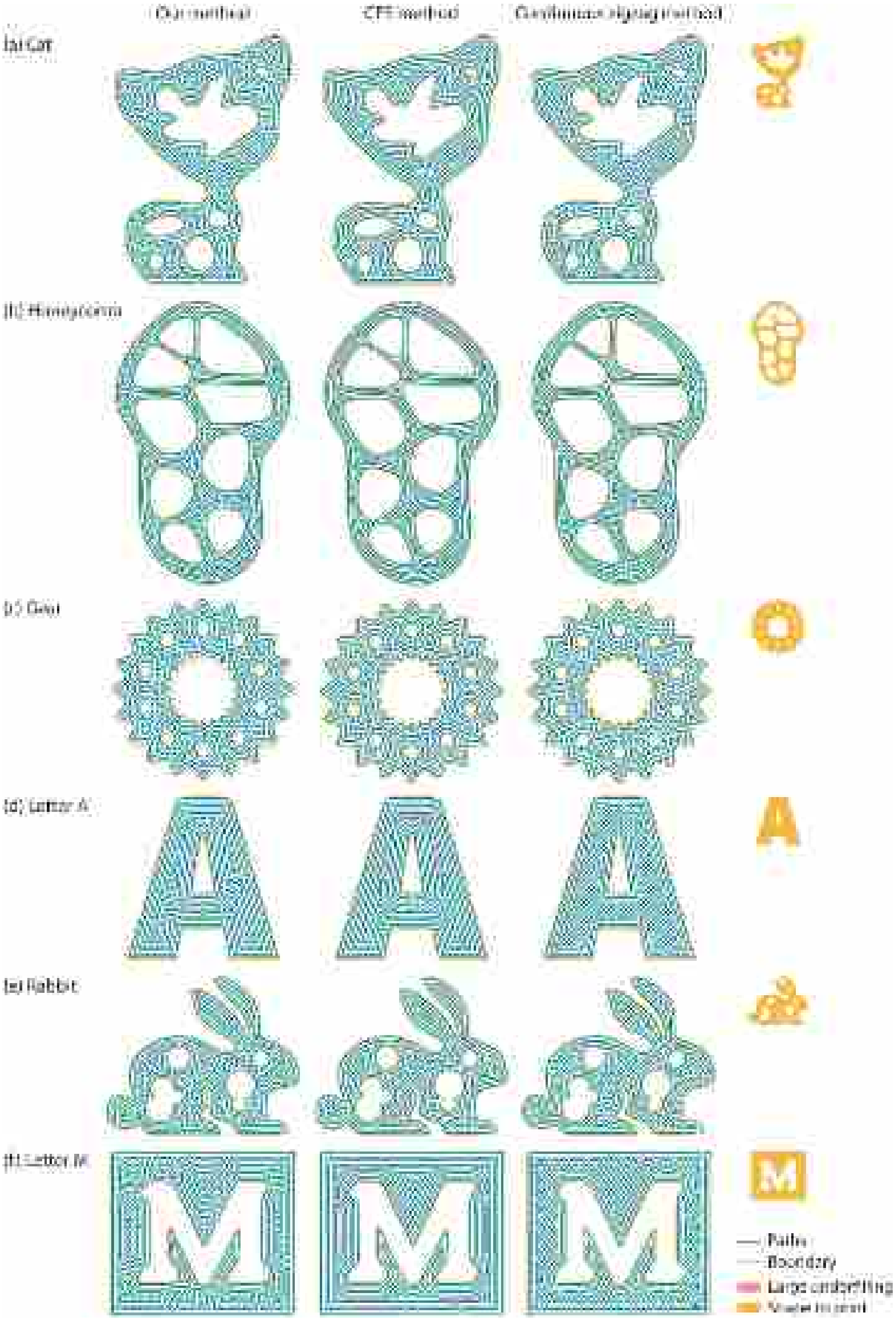

Fig. 15. Six examples are used to compare three continuous toolpath methods: the proposed hybrid method, the CFS method [26], and the continuous zigzag method [48].

4.1.4. *Printing time*

Printing time is another crucial factor for AM processes. The generated toolpaths are printed with a nozzle diameter of 2 mm and a nozzle movement speed of 0.03 m/s. Each 2D toolpath is duplicated on three layers to minimize the contribution of other factors to the total printing time. In the Gcode file, points are sampled equally at a distance of half nozzle diameter to avoid inconsistent filament width between straight and curvy toolpath areas. Table 2c compares the total printing time between different methods. Without needing travel paths, the three continuous toolpaths achieve roughly 4–13% save in printing time than the conventional zigzag and contour-parallel methods. The proposed method is comparable but takes a slightly longer time (1–2%) than the other two continuous toolpath algorithms; However, this is justifiable as toolpaths in the proposed method are extended to cover underfillings areas.

4.1.5. *Computational time*

A comparison of the computational time from different methods is

Table 1
Comparing the print quality of different methods based on four criteria: overfilling ratio, underfilling ratio, number of large gaps, and size of the largest gap. The five methods are abbreviated as: the proposed hybrid method (H), connected Fermat spirals (CFS), the continuous zigzag method (CZ), zigzag method (Z), and contour-parallel method (C).

Factor	(a) Overfilling ratio (%)					(b) Underfilling ratio (%)				
Input	H	CFS	CZ	Z	C	H	CFS	CZ	Z	C
Cat	1.4	1.3	**1.2**	1.7	1.9	**2.2**	3.8	4.7	3.6	3.1
Honeycomb	2.2	2.2	**1.7**	2.0	2.2	**2.1**	4.7	4.7	5.3	4.3
Gear	2.6	2.6	**1.0**	1.5	2.1	**1.4**	4.5	4.8	5.4	5.1
Rabbit	2.0	1.9	2.3	**1.0**	2.5	**1.7**	3.7	3.7	4.0	3.0
Letter A	0.5	0.6	**0.4**	1.1	0.7	**0.9**	2.0	2.8	2.0	1.8
Letter M	**0.9**	1.0	1.5	1.3	**0.9**	**1.7**	3.0	3.4	2.6	3.3

Factor	(c) Number of large gaps					(d) Size of the largest gap (%)				
Input	H	CFS	CZ	Z	C	H	CFS	CZ	Z	C
Cat	**0**	17	22	18	14	**0.03**	0.46	0.28	0.21	0.40
Honeycomb	**0**	23	20	25	25	**0.02**	0.55	0.19	0.25	0.56
Gear	**0**	22	21	44	23	**0.02**	0.21	0.19	0.23	0.22
Rabbit	**0**	20	14	23	18	**0.03**	0.37	0.31	0.25	0.38
Letter A	**0**	6	12	15	6	**0.02**	0.43	0.14	0.17	0.39
Letter M	**0**	11	9	12	13	**0.02**	0.41	0.37	0.16	0.69

Table 2
Comparing the efficiency of different methods based on four criteria: number of path segments, number of sharp turns, printing time, and computational time. The five methods are abbreviated as: the proposed hybrid method (H), connected Fermat spirals (CFS), the continuous zigzag method (CZ), zigzag method (Z), and contour-parallel method (C).

Factor	(a) *number of path segments*					(b) *Number of sharp turns (%)*				
Input	H	CFS	CZ	Z	C	H	CFS	CZ	Z	C
Cat	**1**	**1**	**1**	18	36	**0.1**	0.4	0.5	2.3	0.4
Honeycomb	**1**	**1**	**1**	21	37	**0.1**	0.3	0.6	3.1	0.3
Gear	**1**	**1**	**1**	33	47	**0.2**	0.6	1.1	3.1	0.3
Rabbit	**1**	**1**	**1**	17	27	**0.1**	0.4	0.8	3.5	0.3
Letter A	**1**	**1**	**1**	5	14	**0.1**	**0.1**	0.3	1.3	**0.1**
Letter M	**1**	**1**	**1**	7	18	**0.1**	0.2	0.6	1.8	**0.1**

Factor	(c) Printing time (s)					(d) Computational time (ms)				
Input	H	CFS	CZ	Z	C	H	CFS	CZ	Z	C
Cat	439	437	**433**	467	475	724	1816	817	795	**60**
Honeycomb	461	456	**453**	480	515	1247	2142	1359	923	**99**
Gear	397	391	**387**	432	459	1155	2987	1266	1622	**136**
Rabbit	372	**367**	368	387	416	1070	1427	959	873	**88**
Letter A	370	366	**364**	385	392	243	1227	223	170	**18**
Letter M	449	448	**447**	475	500	652	2161	667	495	**28**

summarised in Table 2d. Thanks to their simplicity, discontinuous toolpath algorithms are much more computationally efficient. Without post-processing, the computational time of the proposed method is comparable to the other two algorithms in the literature. Allowing post-processing generally signifies a prolonged computational time of three to four times. A similar observation is noted in previous work [26].

4.1.6. *Strength and limitation*

After numerically comparing the performance of different methods, the pros and cons of the proposed method are concluded.

Strength:

- Having a minimum number and size of underfilling areas leads to excellent print quality.
- Compared with discontinuous toolpath methods, the proposed hybrid method saves 4–13% printing time.
- Compared with other algorithms, much fewer sharp turns are generated in the proposed method.

Limitation:

- Allowing post-processing can considerably increase the computational time.
- Compared with the CFS method, the proposed method creates fewer straight segments and more curvy lines, which can be disadvantageous in high-speed printing due to dynamic movement conditions (deceleration in curvy toolpaths).

4.2. *Results with partial infill*

Fig. 16 presents the toolpaths for the same six examples under two sets of partial infill setups: 50% infill orientated at 0° and 25% infill orientated at 45°. Toolpaths on the rectangular grid are trimmed and joined into globally continuous paths, allowing hollowed sections for weight reduction. Small underfilling areas generated on the boundaries are refilled based on the zigzag operation introduced in Section 3.2. Despite being innovative and efficient, the proposed method is reported for three limitations:

- Without post-processing, sharp turns can be observed on the generated toolpaths.
- Depending on the geometry and grid position, some toolpaths might be placed too close to the boundaries, creating overfilling areas.
- If the infill ratio is too small (grid spacing is too large), internal boundaries may not intersect with the grid. In this scenario, such interval boundaries will be left unconnected from the continuous toolpath.

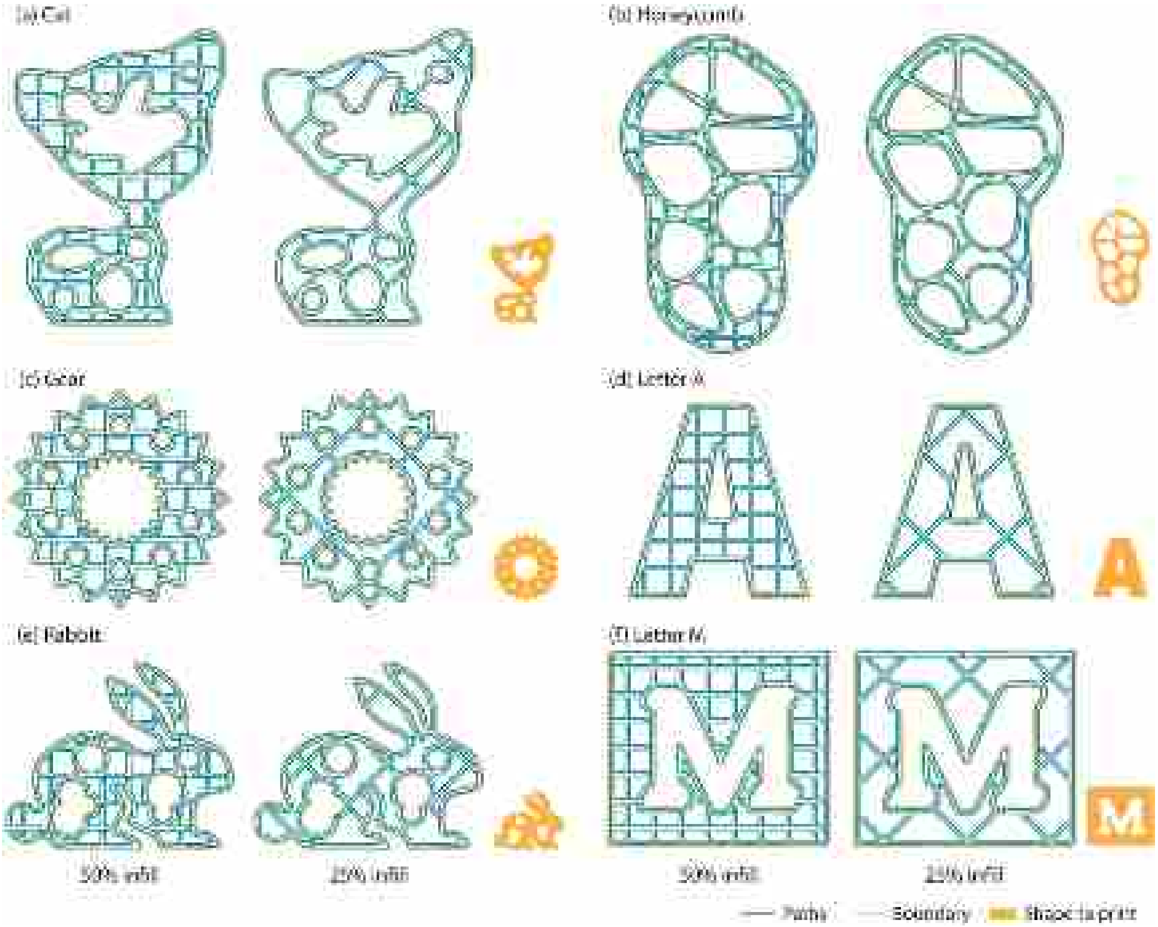

Fig. 16. Six examples with partial infill under two setups: 50% infill with $\theta = 0^\circ$ (left) and 25% infill with $\theta = 45^\circ$ (right).

Future work could be developed to tackle the reported problems.

4.3. More results

Ten more results are illustrated in Fig. 17, and their performances are listed in Table 3. Most of the presented results achieve great overfilling and underfilling ratios, except for the pear and Mobius examples. Geometrically speaking, those two examples have much thinner walls. As a continuous toolpath necessitates both entry and exit paths for a route, thinner walls lead to two narrowly spaced paths with overfilling. The algorithm's double offset and outward contour schemes prevent creating toolpaths in narrow regions (except for the boundary contour layer). As a result, small gaps can be found near narrow boundaries, such as the tail of the airplane example. A remedy to this issue is to allow zigzag operation extending from the outermost toolpath on the boundary contour layer. However, this may result in a serrated boundary profile and should be chosen wisely depending on the designers' preference.

5. Experiments

The proposed hybrid method is validated by two experiments: topology optimized table printed with TPU and topology optimized chair printed with 3DCP. Research attention has recently been drawn to the integration between AM and topology optimized structures [73–75], whose geometrical complexity typically prohibits their realization in traditional ways. This section introduces two self-supporting geometries created based on the authors' previous work [76]. The topology optimization algorithm is developed on the bi-directional topology optimization (BESO) framework [77,78].

5.1. Topology optimized table printed using TPU

As shown in Fig. 18, a topology optimized table is generated for printing using TPU material. The printing process was carried out by a Kuka robotic arm, Kuka KR210 R2700 extra. The TPU printer has a relatively small nozzle of 2 mm, requiring a dense array of toolpaths to print the full-scale table. In order to test the algorithm's robustness in a more challenging scenario, the structure is scaled down by a factor of 0.3 to allow a relatively larger nozzle-to-size ratio. In this case, underfilling regions are visually noticeable and have a more adverse impact on the print quality. The scaled topology optimized table has a dimension of $400\ \text{mm} \times 130\ \text{mm} \times 110\ \text{mm}$ and consists of two mirrored segments (shown as solid and transparent). Each segment was printed from the side (largest boundary profile) towards the middle section to ensure self-support. The use of chemical adhesive fulfilled the bonding of the two segments at the flat middle surfaces. For weight reduction, the top half of each segment was printed with 50% infill; the bottom half was kept at 100% infill as partial infill may not enable self-support due to interior surfaces' overhang limit. As mechanical properties of TPU material can be affected by various processing parameters [79], the printing setups are reported in Table 4.

2D tests were carried out on five different setups: the proposed hybrid method (Fig. 19a), the CFS method (Fig. 19b), the continuous zigzag method (Fig. 19c), the conventional zigzag method (Fig. 19d), and the proposed partial infill strategy (Fig. 19e). The CFS method generated long segments with low curvature but created noticeable narrow gaps in skeletal regions. The continuous zigzag method achieved

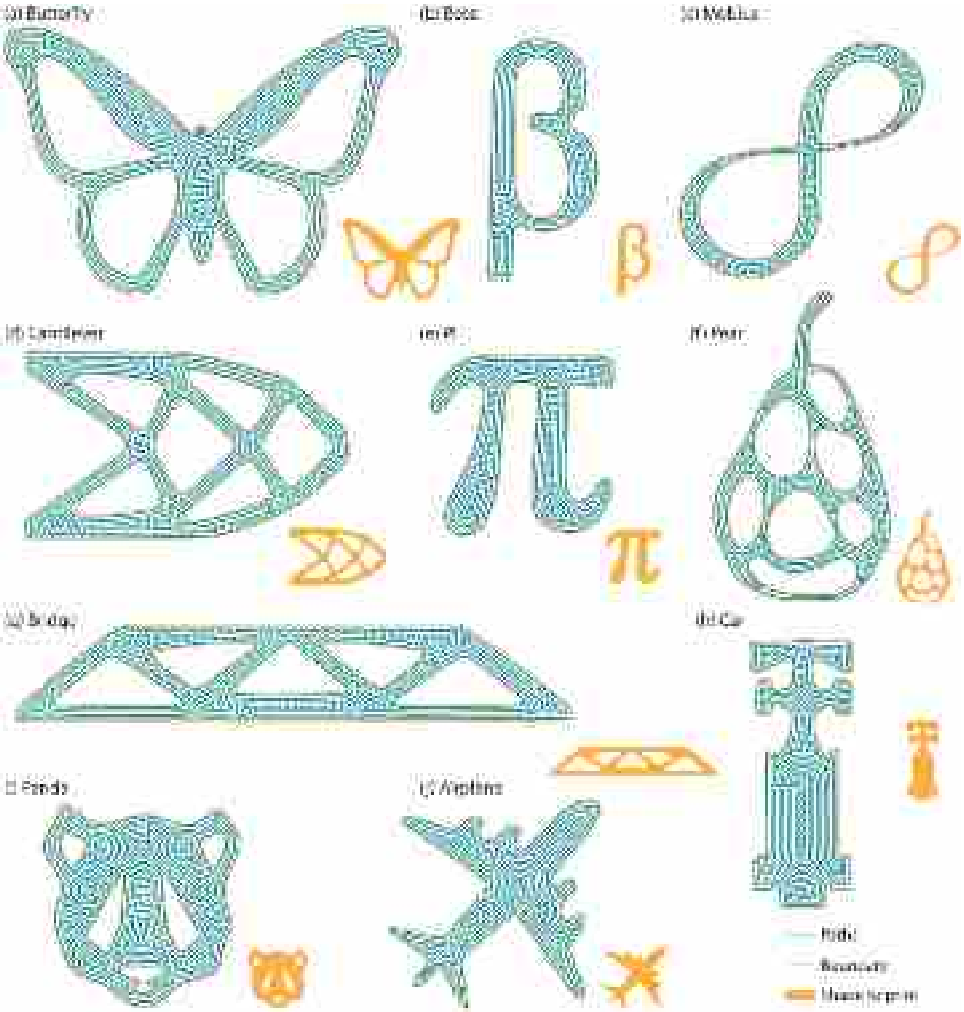

Fig. 17. Illustration of ten more results from the proposed hybrid method.

Table 3
Statistical summary of the ten more results.

Factor	*Overfilling ratio (%)*	*Underfilling ratio (%)*	*Sharp turns (%)*	*Size of largest gap (%)*
Butterfly	2.0	1.5	0.1	0.02
Beta	1.9	1.6	0.1	0.04
Cantilever	1.9	1.2	0.1	0.03
Pi	0.9	1.8	0.1	0.02
Bridge	2.5	1.5	0.1	0.04
Panda	0.7	2.3	0.1	0.04
Airplane	1.9	1.8	0.4	0.04
Pear	5.8	2.3	0.1	0.14
Mobius	4.4	1.7	0.1	0.08
Car	1.4	1.5	0.1	0.04

Fig. 18. A rendered view of the topology optimized table. Two mirrored segments (solid and transparent) were printed and assembled.

Table 4
Printing parameters for the topology optimized table.

Nozzle speed (m/s)	Temperature (°C)	Extrusion rate (g/h)	Nozzle size (mm)	Layer height (mm)
0.03	160	250	2	1.3

better filling near the structure's centrelines but succumbed to poorly covered corners; the reason is previously identified in Section 2.1 as the automatic rounding mechanism of the robotic arm system near sharp turns. The printer cannot support intermittent stops; travel paths between discontinuous segments were assigned with an increased movement speed and removed manually after printing. As a result, bulges and residues can be found in Fig. 19d and entailed extra labor work in the post-processing phase. By comparison, the result from the proposed method achieved the best overall coverage; small overfilling helped the bonding between filaments near corners but did not have a noticeable negative impact on the print quality. The result from the partial infill strategy matched well with the simulation; however, sharp corners created minor gaps near the boundary. As illustrated in Fig. 20, the final 3D outcome printed using our method has achieved good structural infill and surface finish.

5.2. Topology optimized chair printed using 3DCP

A large topology optimized chair with a dimension of 1330 mm ×

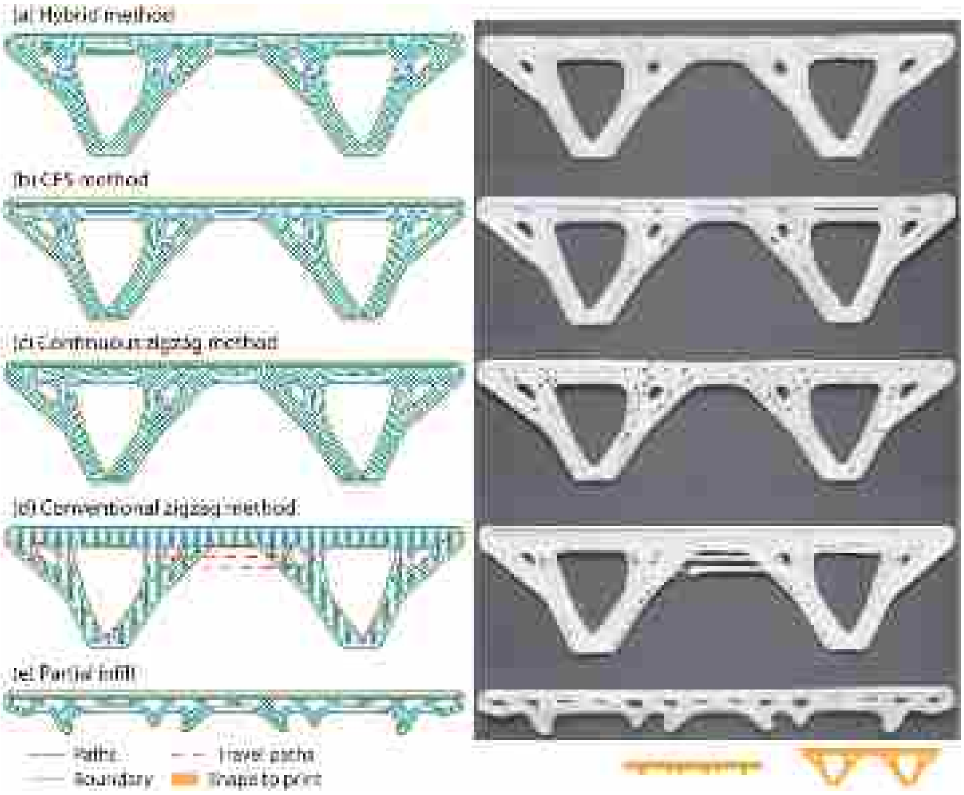

Fig. 19. Toolpaths and 2D print results of the topology optimized table using TPU: (a) the proposed hybrid method; (b) CFS method; (c) continuous zigzag method; (d) conventional zigzag method; (e) partial infill.

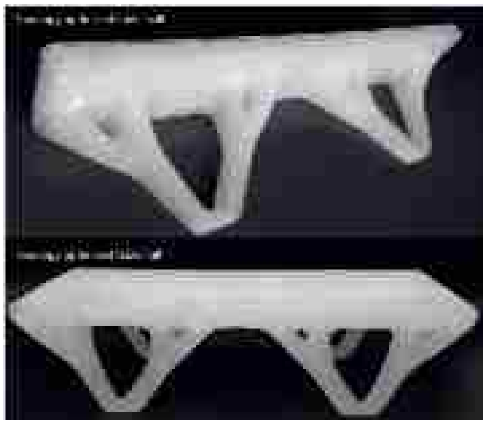

Fig. 20. 3D print result of the topology optimized table: half (top) and whole structure (bottom).

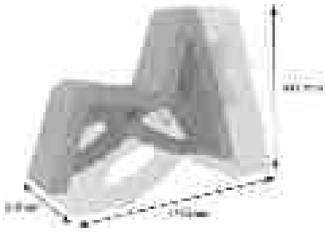

Fig. 21. A rendered view of the topology optimized chair. Two mirrored segments (solid and transparent) were printed and assembled.

Table 5
Mix design used in 3DCP.

Sand (%)	Silica fume (%)	Cement (%)	Water (%)	Superplasticizer (%)	Retarder (%)
45.4	7.8	33.3	12.7	0.6	0.2

Table 6
Printing parameters for the topology optimized chair.

Nozzle speed (m/s)	Extrusion rate (m^3/h)	Nozzle size (mm)	Layer height (mm)
0.1	0.06	15	10

670 mm × 1000 mm was created for 3DCP (Fig. 21). As 3DCP has a more restricted overhang limit, the entire structure was printed with 100% infill to ensure vertical continuity. Under the same concept, two segments were printed individually from the side towards the middle and assembled using chemical adhesive. Materials used in the mix included sand, silica fume, cement, water, polycarboxylate-based superplasticizer, and sodium gluconate retarder; fibers were placed manually during the printing process to enhance the tensile strength of the structure. The robotic arm is Efort ER180, and the mix ratio of raw materials and printing parameters can be found in Table 5 and Table 6.

By selecting the third layer of the 3D structure as the boundary profile, 2D tests are conducted using three different methods: the proposed hybrid method (Fig. 22a), the CFS method (Fig. 22b), and the continuous zigzag method (Fig. 22c). Note that the three printed results in Fig. 22 may not perfectly align because of a slight discrepancy in photo angle. Similar to previous observations, the CFS method was unable to generate a compact infill near the medial axis. On the top left corner, narrowly spaced paths stacked into bulges; A pointed corner

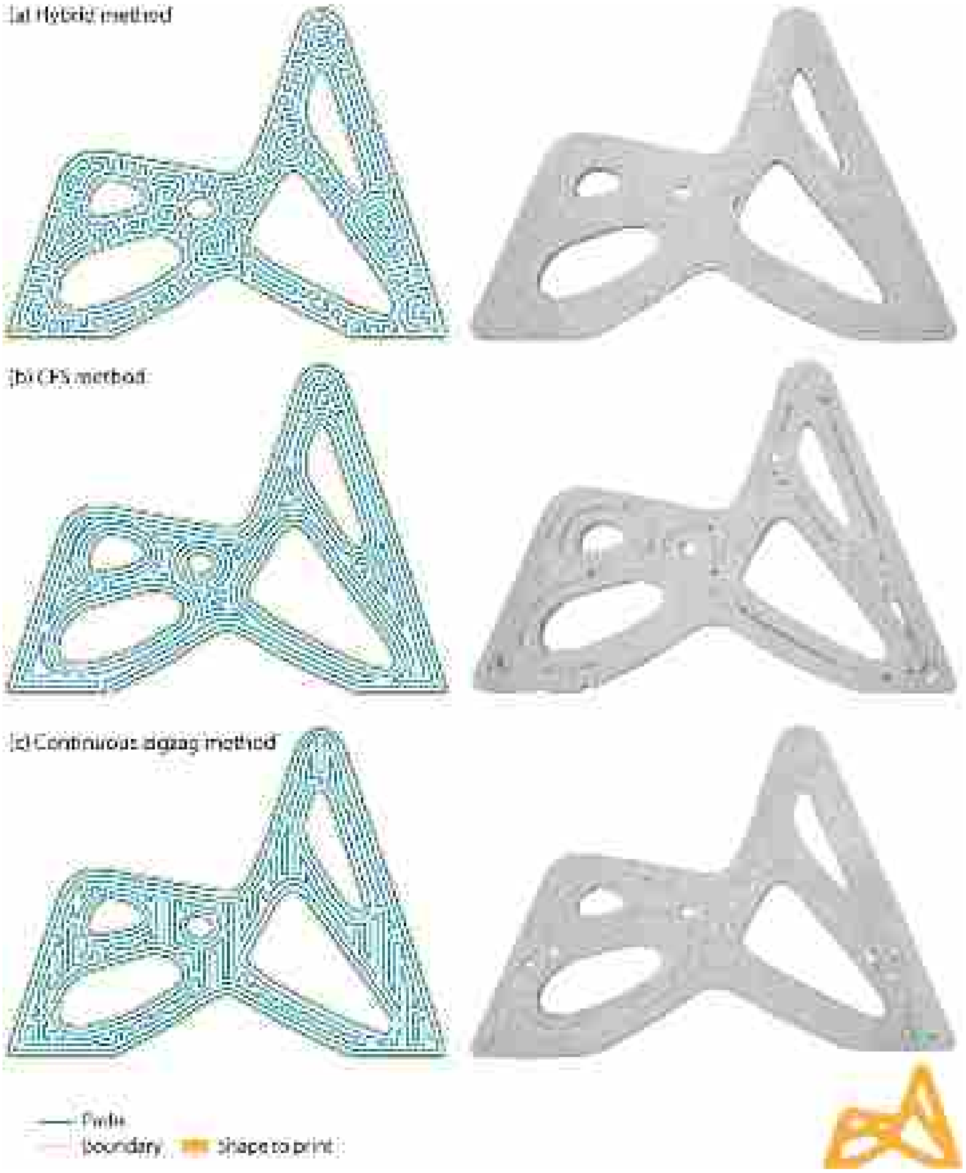

Fig. 22. Toolpaths and 2D print results of the topology optimized chair from three different strategies: (a) the proposed hybrid method; (b) the CFS method; (c) the continuous zigzag method.

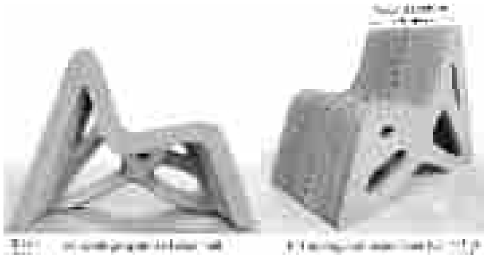

Fig. 23. 3D print result of the topology optimized chair: half (left) and whole structure (right).

generated by the bottleneck effect failed to cover the bottom right region, leaving a substantial local defect. The continuous zigzag path produced satisfactory print quality on the slender beam regions but fell victim to the same sharp corner problem in the bottom right spot. By comparison, the proposed hybrid method showed superior print quality.

With the background removed for clarity, a final 3D outcome is displayed in Fig. 23. The outermost surface has been post-processed to deliver smooth outer surfaces for aesthetics. The example demonstrates how an optimized continuous toolpath can facilitate the fabrication of spatially complex structures while maintaining satisfactory structural integrity and surface quality.

6. Conclusion

This paper presents a novel framework to generate a globally continuous toolpath for both solid and partial infill designs in large format additive manufacturing (LFAM). A hybrid method is proposed for solid infill to create smooth contours as the primary volume-filling paths and zigzag lines to minimize local gaps. The concept is extended for partial infill settings by trimming and joining rectangular grid lines. The robustness and effectiveness of the proposed algorithm are demonstrated by comparing it with other state-of-the-art methods in the literature. The comprehensive comparison clearly shows that the proposed algorithm is superior in delivering better print quality, less sharp turns, and enhanced fabrication efficiency. Two interesting experiments exemplify how continuous toolpaths can promote the integration between topology optimization and LFAM and show that the proposed method outperforms others in print quality and surface finish.

In future work, adaptive height and speed control can be integrated with the proposed hybrid method to reduce the need for zigzag operation and increase overall smoothness. The extension of continuous toolpath from flat surface slices to spatial infill on a double-curved surface is also worth exploring.

CRediT authorship contribution statement

Guowei Ma: Resources. **Li Zhi:** Resources. **Xie Yi Min:** Writing – review & editing, Supervision, Project administration, Funding acquisition. **Wang Li:** Resources. **Shen Wei:** Resources. **Tran Phuong:** Writing – review & editing, Supervision. **Wan Qian:** Resources. **Minghao Bi:** Writing – original draft, Visualization, Validation, Software, Resources, Project administration, Methodology, Investigation, Formal analysis, Data curation, Conceptualization. **Xia Lingwei:** Resources.

Declaration of Competing Interest

The authors declare that they have no known competing financial interests or personal relationships that could have appeared to influence the work reported in this paper.

Acknowledgment

This project was supported by the Australian Research Council (FL190100014, DP200102190) and RMIT University (Research Stipend Scholarship).

Appendix

Post-processing of the continuous toolpath takes a point-based approach. The toolpath is firstly discretized into points with a constant spacing s; endpoints of polylines are included to preserve features such as corners. In this paper, the constant spacing s is selected as $d/4$. Let denote the sampled points in sequential order.

1. Post-processing of underfilling areas

   Each underfilling area pulls the closest sampled point towards its centroid to increase coverage further. The underfilling areas are found by offsetting the continuous toolpath by half nozzle diameter $d/2$. Let P_c and P_p denote the centroid of the underfilling area and its closest point on the continuous path, respectively. P_p is moved towards P_c by a distance of $d_u = |P_cP_p| - d/2$, where d_u and $|P_cP_p|$ denote the moved distance and the distance between the two points, respectively. If d_u is less than d, the moved point is directly linked to P_{p-1} and P_{p+1} to form the new path; otherwise, P_{p-1} and P_{p+1} are averaged with the neighboring points to improve smoothness:

   $$\begin{Bmatrix} P'_{p-1} = \dfrac{P_{p-2} + P'_p}{2} \\ P'_{p+1} = \dfrac{P_{p+2} + P'_p}{2} \end{Bmatrix} \tag{A1}$$

   where P'_{p-1} and P'_{p+1} denote the new points after averaging. It should be noted that the underfilling areas in the post-processing step are considerably small when compared with the nozzle size d. The value of d_u is usually smaller than $3d$, and the adjusted points do not significantly change the topology of the original path.
2. Post-processing of overfilling areas

Post-processing of overfilling areas takes a filter-based approach. With point P_n as the center, a filter ∂R with a radius of $d/2$ is applied to search its neighboring points. All points within the radius except for P_n itself are weighted to find the average point P_{ave}:

$$P_{ave} = \frac{\sum\limits_{\{P_i \in \partial R | P_i \neq P_n\}}^{n} P_i}{n} \tag{A2}$$

where P_i and n denote points within the filter and the number of included points, respectively. Inspired by the mid-point scheme (e.g., $P_{i-1} + P_{i+1} \approx 2P_i$), we project P_{ave} onto the centreline between P_{n-1} and P_{n+1}. The vector $\overline{O}$ from the projected point P'_{ave} towards P_{ave} is used to represent the level of crowdedness in the local region. If all points within the filter are aligned in a straight line, the vector length $|\overline{O}|$ is 0. Conversely, for heavily congested areas or points near sharp corners, P_{ave} is away from P'_{ave} and the vector length $|\overline{O}|$ is significant. To increase smoothness and reduce overlapping, P_n is moved in the opposite direction of $\overline{O}$ at a distance of $|\overline{O}|$. Geometrically speaking, this relocates P_n away from the center of the congested region. All relocated points P'_n will be joined together to form the smoothed tool path.

References

[1] I. Gibson, D. Rosen, B. Stucker, M. Khorasani. Additive manufacturing technologies, 3rd ed., Springer, Cham, 2021 https://doi.org/10.1007/978-3-030-56127-7.

[2] A. Pajonk, A. Prieto, U. Blum, U. Knaack, Multi-material additive manufacturing in architecture and construction: a review, J. Build. Eng. (2021), 103603, https://doi.org/10.1016/j.jobe.2021.103603.

[3] R. Leal, F.M. Barreiros, L. Alves, F. Romeiro, J.C. Vasco, M. Santos, C. Marto, Additive manufacturing tooling for the automotive industry, Int. J. Adv. Manuf. Technol. 92 (2017) 1671–1676, https://doi.org/10.1007/s00170-017-0239-8.

[4] F.A.M.M. Gonçalves, A.C. Fonseca, M. Domingos, A. Gloria, A.C. Serra, J.F. J. Coelho, The potential of unsaturated polyesters in biomedicine and tissue engineering: synthesis, structure-properties relationships and additive manufacturing, Prog. Polym. Sci. 68 (2017) 1–34, https://doi.org/10.1016/j.progpolymsci.2016.12.008.

[5] B. Blakey-Milner, P. Gradl, G. Snedden, M. Brooks, J. Pitot, E. Lopez, M. Leary, F. Berto, A. du Plessis, Metal additive manufacturing in aerospace: a review, Mater. Des. 209 (2021), 110008, https://doi.org/10.1016/j.matdes.2021.110008.

[6] H. Shen, L. Pan, J. Qian, Research on large-scale additive manufacturing based on multi-robot collaboration technology, Addit. Manuf. 30 (2019), 100906, https://doi.org/10.1016/j.addma.2019.100906.

[7] S. Roy, B. Silwal, A. Nycz, M. Noakes, E. Cakmak, P. Nandwana, Y. Yamamoto, Investigating the effect of different shielding gas mixtures on microstructure and mechanical properties of 410 stainless steel fabricated via large scale additive manufacturing, Addit. Manuf. 38 (2021), 101821, https://doi.org/10.1016/j.addma.2020.101821.

[8] B.G. Compton, B.K. Post, C.E. Duty, L. Love, V. Kunc, Thermal analysis of additive manufacturing of large-scale thermoplastic polymer composites, Addit. Manuf. 17 (2017) 77–86, https://doi.org/10.1016/j.addma.2017.07.006.

[9] F. Gobbin, H. Elsayed, A. Italiano, J. Adrien, P. Colombo, E. Maire, Large scale additive manufacturing of artificial stone components using binder jetting and their X-ray microtomography investigations, Open Ceram. 7 (2021), 100162, https://doi.org/10.1016/j.oceram.2021.100162.

[10] K.M.M. Billah, J. Heineman, P. Mhatre, A. Roschli, B. Post, V. Kumar, S. Kim, G. Haye, J. Jackson, Z. Skelton, V. Kunc, A.A. Hassen, Large-scale additive manufacturing of self-heating molds, Addit. Manuf. 47 (2021), 102282, https://doi.org/10.1016/j.addma.2021.102282.

[11] N.D. Sanandiya, Y. Vijay, M. Dimopoulou, S. Dritsas, J.G. Fernandez, Large-scale additive manufacturing with bioinspired cellulosic materials, Sci. Rep. 8 (2018) 8642, https://doi.org/10.1038/s41598-018-26985-2.

[12] L. Gardner, P. Kyvelou, G. Herbert, C. Buchanan, Testing and initial verification of the world's first metal 3D printed bridge, J. Constr. Steel Res. 172 (2020), 106233, https://doi.org/10.1016/j.jcsr.2020.106233.

[13] N. Gaudillière, R. Duballet, C. Bouyssou, A. Mallet, P. Roux, M. Zakeri, J. Dirrenberger, Large-Scale additive manufacturing of Ultra-high-performance concrete of integrated formwork for truss-shaped pillars, in: J. Willmann, P. Block, M. Hutter, K. Byrne, T. Schork (Eds.), ROBARCH 2018 Robot. Fabr. Archit. Art Des. 2018, Springer, Cham, 2019, pp. 459–472, https://doi.org/10.1007/978-3-319-92294-2_35.

[14] A. Paolini, S. Kollmannsberger, E. Rank, Additive manufacturing in construction: a review on processes, applications, and digital planning methods, Addit. Manuf. 30 (2019), 100894, https://doi.org/10.1016/j.addma.2019.100894.

[15] A. Diourté, F. Bugarin, C. Bordreuil, S. Segonds, Continuous three-dimensional path planning (CTPP) for complex thin parts with wire arc, Addit. Manuf., Addit. Manuf. 37 (2021), 101622, https://doi.org/10.1016/j.addma.2020.101622.

[16] J. Allum, J. Kitzinger, Y. Li, V.V. Silberschmidt, A. Gleadall, ZigZagZ: improving mechanical performance in extrusion additive manufacturing by nonplanar toolpaths, Addit. Manuf. 38 (2021), 101715, https://doi.org/10.1016/j.addma.2020.101715.

[17] G.Q. Jin, W.D. Li, L. Gao, An adaptive process planning approach of rapid prototyping and manufacturing, Robot. Comput. Integr. Manuf. 29 (2013) 23–38, https://doi.org/10.1016/j.rcim.2012.07.001.

[18] J. Jiang, X. Xu, J. Stringer, Support structures for additive manufacturing: a review, J. Manuf. Mater. Process. 2 (2018) 64, https://doi.org/10.3390/jmmp2040064.

[19] J. Jiang, J. Stringer, X. Xu, Support optimization for flat features via path planning in additive manufacturing, 3D Print, Addit. Manuf. 6 (2018) 171–179, https://doi.org/10.1089/3dp.2017.0124.

[20] J. Jiang, S.T. Newman, R.Y. Zhong, A review of multiple degrees of freedom for additive manufacturing machines, Int. J. Comput. Integr. Manuf. 34 (2021) 195–211, https://doi.org/10.1080/0951192X.2020.1858510.

[21] L. Xia, S. Lin, G. Ma, Stress-based tool-path planning methodology for fused filament fabrication, Addit. Manuf. 32 (2020), 101020, https://doi.org/10.1016/j.addma.2019.101020.

[22] X. Chen, G. Fang, W.-H. Liao, C.C.L. Wang, Field-based toolpath generation for 3D printing continuous fibre reinforced thermoplastic composites, Addit. Manuf. 49 (2022), 102470, https://doi.org/10.1016/j.addma.2021.102470.

[23] P. Delfs, M. Tows, H.-J. Schmid, Optimized build orientation of additive manufactured parts for improved surface quality and build time, Addit. Manuf. 12 (2016) 314–320, https://doi.org/10.1016/j.addma.2016.06.003.

[24] F. Ren, Y. Sun, D. Guo, Combined reparameterization-based spiral toolpath generation for five-axis sculptured surface machining, Int. J. Adv. Manuf. Technol. 40 (2008) 760–768, https://doi.org/10.1007/s00170-008-1385-9.

[25] B. Zhou, J. Zhao, L. Li, CNC double spiral tool-path generation based on parametric surface mapping, Comput. Des. 67– 68 (2015) 87–106, https://doi.org/10.1016/j.cad.2015.06.005.

[26] H. Zhao, F. Gu, Q.-X. Huang, J. Garcia, Y. Chen, C. Tu, B. Benes, H. Zhang, D. Cohen-Or, B. Chen, Connected fermat spirals for layered fabrication, ACM Trans. Graph 35 (2016) 1–10, https://doi.org/10.1145/2897824.2925958.

[27] J.G. Griffiths, Toolpath based on Hilbert's curve, Comput. Aided Des. 26 (1994) 839–844, https://doi.org/10.1016/0010-4485(94)90098-1.

[28] J. Jiang, Y. Ma, Path planning strategies to optimize accuracy, quality, build time and material use in additive manufacturing: a review, Micromachines 11 (2020) 633, https://doi.org/10.3390/mi11070633.

[29] X. Wang, K.-M.M. Tam, A. Beaudouin-Mackay, B. Hoyle, M. Mason, Z. Guo, W. Gao, C. Li, W. Zhu, Z. Karsan, G.T.-C. Kao, L. Zhang, H. Chai, P.F. Yuan, P. Block, 3D-printed bending-active formwork for shell structures, in: P.F. Yuan, Y. M. Xie, N. Leach, J. Yao, X. Wang (Eds.), Archit. Intell., Springer, Singapore, 2020, pp. 295–314, https://doi.org/10.1007/978-981-15-6568-7_18.

[30] Y. He, Y. Zhang, C. Zhang, H. Zhou, Energy-saving potential of 3D printed concrete building with integrated living wall, Energy Build. 222 (2020), 110110, https://doi.org/10.1016/j.enbuild.2020.110110.

[31] X. Zhang, M. Li, J.H. Lim, Y. Weng, Y.W.D. Tay, H. Pham, Q.-C. Pham, Large-scale 3D printing by a team of mobile robots, Autom. Constr. 95 (2018) 98–106, https://doi.org/10.1016/j.autcon.2018.08.004.

[32] B.B.M. Kumar, Y.C. Hsueh, Z. Xin, D. Luo, Process and evaluation of automated robotic fabrication system for in-situ structure confinement, in: P.F. Yuan, H. Chai, C. Yan, N. Leach (Eds.), Proc. 2021 Digit. Futur., Springer Singapore, Singapore, 2022, pp. 368–379.

[33] V. Mechtcherine, V.N. Nerella, F. Will, M. Näther, J. Otto, M. Krause, Large-scale digital concrete construction – CONPrint3D concept for on-site, monolithic 3D-printing, Autom. Constr. 107 (2019), 102933, https://doi.org/10.1016/j.autcon.2019.102933.

[34] T.T. Le, S.A. Austin, S. Lim, R.A. Buswell, A.G.F. Gibb, T. Thorpe, Mix design and fresh properties for high-performance printing concrete, Mater. Struct. 45 (2012) 1221–1232, https://doi.org/10.1617/s11527-012-9828-z.

[35] D. Zhang, D. Zhou, G. Zhang, G. Shao, L. Li, 3D printing lunar architecture with a novel cable-driven printer, Acta Astronaut 189 (2021) 671–678, https://doi.org/10.1016/j.actaastro.2021.09.034.

[36] N. Labonnote, A. Rønnquist, B. Manum, P. Rüther, Additive construction: State-of-the-art, challenges and opportunities, Autom. Constr. 72 (2016) 347–366, https://doi.org/10.1016/j.autcon.2016.08.026.

[37] B. Sencer, K. Ishizaki, E. Shamoto, A curvature optimal sharp corner smoothing algorithm for high-speed feed motion generation of NC systems along linear tool paths, Int. J. Adv. Manuf. Technol. 76 (2015) 1977–1992, https://doi.org/10.1007/s00170-014-6386-2.

[38] J. Liu, V. Nguyen-Van, B. Panda, K. Fox, A. du Plessis, P. Tran, Additive manufacturing of sustainable construction materials and form-finding structures: a review on recent progresses, 3D Print, Addit. Manuf. (2021), https://doi.org/10.1089/3dp.2020.0331.

[39] V.N. Nerella, M. Näther, A. Iqbal, M. Butler, V. Mechtcherine, Inline quantification of extrudability of cementitious materials for digital construction, Cem. Concr. Compos. 95 (2019) 260–270, https://doi.org/10.1016/j.cemconcomp.2018.09.015.

[40] N. Roussel, Rheological requirements for printable concretes, Cem. Concr. Res. 112 (2018) 76–85, https://doi.org/10.1016/j.cemconres.2018.04.005.

[41] T.A.M. Salet, Z.Y. Ahmed, F.P. Bos, H.L.M. Laagland, Design of a 3D printed concrete bridge by testing, Virtual Phys. Prototyp. 13 (2018) 222–236, https://doi.org/10.1080/17452759.2018.1476064.

[42] N. Hack, K. Dörfler, A.N. Walzer, T. Wangler, J. Mata-Falcón, N. Kumar, J. Buchli, W. Kaufmann, R.J. Flatt, F. Gramazio, M. Kohler, Structural stay-in-place formwork for robotic in situ fabrication of non-standard concrete structures: a real scale architectural demonstrator, Autom. Constr. 115 (2020), 103197, https://doi.org/10.1016/j.autcon.2020.103197.

[43] J. Xiao, G. Ji, Y. Zhang, G. Ma, V. Mechtcherine, J. Pan, L. Wang, T. Ding, Z. Duan, S. Du, Large-scale 3D printing concrete technology: current status and future opportunities, Cem. Concr. Compos. 122 (2021), 104115, https://doi.org/10.1016/j.cemconcomp.2021.104115.

[44] L. Pham, G. Lu, P. Tran, Influences of printing pattern on mechanical performance of three-dimensional-printed fiber-reinforced concrete, 3D Print, Addit. Manuf. (2020), https://doi.org/10.1089/3dp.2020.0172.

[45] D. Ding, Z. Pan, D. Cuiuri, H. Li, A tool-path generation strategy for wire and arc additive manufacturing, Int. J. Adv. Manuf. Technol. 73 (2014) 173–183, https://doi.org/10.1007/s00170-014-5808-5.

[46] Y. Jin, Y. He, G. Fu, A. Zhang, J. Du, A non-retraction path planning approach for extrusion-based additive manufacturing, Robot. Comput. Integr. Manuf. 48 (2017) 132–144, https://doi.org/10.1016/j.rcim.2017.03.008.

[47] Y. Jin, Y. He, J. Fu, W. Gan, Z. Lin, Optimization of tool-path generation for material extrusion-based additive manufacturing technology, Addit. Manuf. 1– 4 (2014) 32–47, https://doi.org/10.1016/j.addma.2014.08.004.

[48] L. Xia, G. Ma, F. Wang, G. Bai, Y.M. Xie, W. Xu, J. Xiao, Globally continuous hybrid path for extrusion-based additive manufacturing, Autom. Constr. 137 (2022), 104175, https://doi.org/10.1016/j.autcon.2022.104175.

[49] R. Dwivedi, R. Kovacevic, Automated torch path planning using polygon subdivision for solid freeform fabrication based on welding, J. Manuf. Syst. 23 (2004) 278–291, https://doi.org/10.1016/S0278-6125(04)80040-2.

[50] M. Held, G. Lukács, L. Andor, Pocket machining based on contour-parallel tool paths generated by means of proximity maps, Comput. Des. 26 (1994) 189–203, https://doi.org/10.1016/0010-4485(94)90042-6.

[51] H. Persson, NC machining of arbitrarily shaped pockets, Comput. Des. 10 (1978) 169–174, https://doi.org/10.1016/0010-4485(78)90141-0.

[52] M. Held, VRONI: an engineering approach to the reliable and efficient computation of Voronoi diagrams of points and line segments, Comput. Geom. 18 (2001) 95–123, https://doi.org/10.1016/S0925-7721(01)00003-7.

[53] R. Kimmel, A.M. Bruckstein, Shape offsets via level sets, Comput. Des. 25 (1993) 154–162, https://doi.org/10.1016/0010-4485(93)90040-U.

[54] Y.-L. Lai, J.-S. Wu, J.-P. Hung, J.-H. Chen, A simple method for invalid loops removal of planar offset curves, Int. J. Adv. Manuf. Technol. 27 (2005) 1153–1162, https://doi.org/10.1007/s00170-004-2318-x.

[55] X.-Z. Liu, J.-H. Yong, G.-Q. Zheng, J.-G. Sun, An offset algorithm for polyline curves, Comput. Ind. 58 (2007) 240–254, https://doi.org/10.1016/j.compind.2006.06.002.

[56] B.K. Choi, S.C. Park, A pair-wise offset algorithm for 2D point-sequence curve, Comput. Des. 31 (1999) 735–745, https://doi.org/10.1016/S0010-4485(99)00060-3.

[57] H.-C. Kim, S.-G. Lee, M.-Y. Yang, A new offset algorithm for closed 2D lines with islands, Int. J. Adv. Manuf. Technol. 29 (2005) 1169–1177, https://doi.org/10.1007/s00170-005-0013-1.

[58] Z. Lin, J. Fu, Y. He, W. Gan, A robust 2D point-sequence curve offset algorithm with multiple islands for contour-parallel tool path, Comput. Des. 45 (2013) 657–670, https://doi.org/10.1016/j.cad.2012.09.002.

[59] B. Vatti, A generic solution to polygon clipping, Commun. Acm. 35 (1992) 56–63, https://doi.org/10.1145/129902.129906.

[60] M.K. Agoston, Computer graphics and geometric modeling. Implementation and algorithms, Springer,, London, 2005, https://doi.org/10.1007/b138805.

[61] A. Johnson, Clipper, (2014). http://www.angusj.com/delphi/clipper.php (Accessed 17 November 2021).

[62] Z. Lin, J. Fu, H. Shen, X. Yao, Smooth contour-parallel tool path generation for high-speed machining through a dual offset procedure, Int. J. Adv. Manuf. Technol. 81 (2015) 1233–1245, https://doi.org/10.1007/s00170-015-7275-z.

[63] K. Xu, Y. Li, B. Xiang, Image processing-based contour parallel tool path optimization for arbitrary pocket shape, Int. J. Adv. Manuf. Technol. 102 (2018) 1091–1105, https://doi.org/10.1007/s00170-018-3016-4.

[64] X. Zhai, F. Chen, Path planning of a type of porous structures for additive manufacturing, Comput. Des. 115 (2019) 218–230, https://doi.org/10.1016/j.cad.2019.06.002.

[65] S. Shaikh, N. Kumar, P.K. Jain, P. Tandon, Hilbert curve based toolpath for FDM process, in: D.K. Mandal, C.S. Syan (Eds.), CAD/CAM, Robot. Factories Futur., Springer India, New Delhi, 2016, pp. 751–759.

[66] T. Kuipers, J. Wu, C.L. Wang, CrossFill: foam structures with graded density for continuous material extrusion, Comput. Des. 114 (2019) 37–50, https://doi.org/10.1016/j.cad.2019.05.003.

[67] S. Lin, L. Xia, G. Ma, S. Zhou, Y.M. Xie, A maze-like path generation scheme for fused deposition modeling, Int. J. Adv. Manuf. Technol. 104 (2019) 1509–1519, https://doi.org/10.1007/s00170-019-03986-7.

[68] D. Ding, Z. Pan, D. Cuiuri, H. Li, N. Larkin, Adaptive path planning for wire-feed additive manufacturing using medial axis transformation, J. Clean. Prod. 133 (2016) 942–952, https://doi.org/10.1016/j.jclepro.2016.06.036.

[69] Y. Jin, J. Du, Z. Ma, A. Liu, Y. He, An optimization approach for path planning of high-quality and uniform additive manufacturing, Int. J. Adv. Manuf. Technol. 92 (2017) 651–662, https://doi.org/10.1007/s00170-017-0207-3.

[70] T. Kuipers, E. Doubrovski, J. Wu, C.L. Wang, A framework for adaptive width control of dense contour-parallel toolpaths in fused deposition modeling, Comput. Des. 128 (2020), 102907, https://doi.org/10.1016/j.cad.2020.102907.

[71] J. Etienne, N. Ray, D. Panozzo, S. Hornus, C. Wang, J. Martínez, S. McMains, M. Alexa, B. Wyvill, S. Lefebvre, CurviSlicer: Slightly curved slicing for 3-axis printers, ACM Trans. Graph. 38 (2019) 1–11, https://doi.org/10.1145/3306346.3323022.

[72] T. Zhang, X. Chen, G. Fang, Y. Tian, C.C.L. Wang, Singularity-aware motion planning for multi-axis additive manufacturing, IEEE Robot. Autom. Lett. 6 (2021) 6172–6179, https://doi.org/10.1109/LRA.2021.3091109.

[73] Y. Xiong, S. Yao, Z.-L. Zhao, Y.M. Xie, A new approach to eliminating enclosed voids in topology optimization for additive manufacturing, Addit. Manuf. 32 (2020), 101006, https://doi.org/10.1016/j.addma.2019.101006.

[74] J. Ma, Z. Li, Z.-L. Zhao, Y.M. Xie, Creating novel furniture through topology optimization and advanced manufacturing, Rapid Prototyp. J. 27 (2021) 1749–1758, https://doi.org/10.1108/RPJ-03-2021-0047.

[75] M. Bi, P. Tran, Y.M. Xie, Topology optimization of 3D continuum structures under geometric self-supporting constraint, Addit. Manuf. 36 (2020), 101422, https://doi.org/10.1016/j.addma.2020.101422.

[76] M. Bi, P. Tran, L. Xia, G. Ma, Y.M. Xie, Topology optimization for 3D concrete printing with various manufacturing constraints, Addit. Manuf. (2022).

[77] X. Huang, Y.M. Xie, Bi-directional evolutionary topology optimization of continuum structures with one or multiple materials, Comput. Mech. 43 (2008) 393–401, https://doi.org/10.1007/s00466-008-0312-0.

[78] X. Huang, Y.M. Xie, Evolutionary Topology Optimization of Continuum Structures: Methods and Applications, John Wiley & Sons, Ltd, Chichester, England, 2010, https://doi.org/10.1002/9780470689486.

[79] T. Xu, W. Shen, X. Lin, Y.M. Xie, Mechanical properties of additively manufactured thermoplastic polyurethane (TPU) material affected by various processing parameters, Polymers 12 (2020) 3010, https://doi.org/10.3390/polym12123010.